American Mineralogist, Volume 89, pages 405–420, 2004

# Structural variations in the brownmillerite series $Ca_2(Fe_{2-x}Al_x)O_5$: Single-crystal X-ray diffraction at 25 °C and high-temperature X-ray powder diffraction (25 °C ≤ $T$ ≤ 1000 °C)

GÜNTHER J. REDHAMMER,[1,*] GEROLD TIPPELT,[2] GEORG ROTH,[1] AND GEORG AMTHAUER[2]

[1]Institute of Crystallography, Rheinisch-Westfalische Technische Hochschule Aachen, Jagerstrasse 17/19, D-52056 Aachen, Germany
[2]Institute of Mineralogy, University of Salzburg, Hellbrunnerstrasse 34, A-5020 Salzburg, Austria
[3]Corresponding address: Neuhofen im Innkreis 224/1, A-4910 Ried im Innkreis, Austria

## ABSTRACT

A total of 30 synthetic samples of the $Ca_2Fe_{2-x}Al_xO_5$, 0.00 ≤ $x$ ≤ 1.34 solid solution series have been investigated by single crystal X-ray diffraction at 25 °C. Pure $Ca_2Fe_2O_5$ and samples up to $x$ = 0.56 have space group *Pnma*, $Z$ = 4, whereas samples with $x$ > 0.56 show *I*2*mb* symmetry, $Z$ = 4. The substitution of $Fe^{3+}$ by the smaller $Al^{3+}$ cation decreases unit-cell parameters and average octahedral and tetrahedral bond lengths and induces distinct changes in the O-atom coordination of the interstitial Ca atom. Discontinuities in the structural parameters vs. the $Al^{3+}_{tot}$ content and changes in slope of these quantities are associated with the phase transition. The essential difference between the two modifications is the cation-O atom-cation angle within the planes of corner sharing octahedra, which is close to 180° in *I*2*mb*, but ≈184° in the *Pnma* phase, and the existence of two different orientations of the tetrahedral chains in *Pnma* as opposed to one in *I*2*mb*. At low overall $Al^{3+}$ concentrations $Al^{3+}$ preferentially enters the tetrahedral site until ≈2/3 of it is filled. Additional $Al^{3+}$ cations, substituted for $Fe^{3+}$, are equally distributed over octahedral and tetrahedral sites. At high temperature pure $Ca_2Fe_2O_5$ transforms to a body-centered structure at 724(4) °C. Substituting $Al^{3+}$ for $Fe^{3+}$ linearly decreases the transition temperature by 15 °C per 0.1 $Al^{3+}$ down to 623(5) °C for $x$ = 0.65.

## INTRODUCTION

Brownmillerite, $Ca_2AlFeO_5$, oxide composition $4CaO·Al_2O_3·Fe_2O_3$ (C4AF in the nomenclature of cement chemistry), is one of the four most common components of ordinary portland cement clinkers (Taylor 1997). It represents one point in an Al/Fe solid solution series, $Ca_2(Fe_{2-x}Al_x)O_5$ with $x$ = 1.0. Hansen et al. (1928) were the first to study the phase relations in the $CaO-Al_2O_3-Fe_2O_3$ system. A great deal of phase analytical and structural work has been devoted to the system since then (e.g., Bertaut et al. 1959; Smith 1962) including a detailed review of the crystal chemistry of $Al^{3+}$-substituted $Ca_2Fe_2O_5$ by Geller et al. (1971). At atmospheric pressure a continuous solid-solution series exists in the compositional range 0.0 ≤ $x$ ≤ 1.4 (e.g., Smith 1962; Geller et al. 1971; Taylor 1997). The $Ca_2(Fe_{2-x}Al_x)O_5$ compounds have orthorhombic symmetry, however, they are not isostructural throughout the complete solid solution series. Samples with compositions less than $x$ = 0.6 were found to have space group *Pnma* (Bertaut et al. 1959; Smith 1962), whereas for samples with $x$ > 0.66 some controversy concerning the exact symmetry exists in the older literature. Smith (1962) proposed space group *Icmm* but subsequently it was discovered that these samples have a slightly modified structure with space group *I*2*mb* (Colville and Geller 1971, 1972).

The crystal structure of pure $Ca_2Fe_2O_5$ was first described by Bertaut et al. (1959) and later re-determined by Colville (1970). In agreement with Smith (1962) it belongs to space group *Pnma* with $a$ = 5.429(1), $b$ = 14.771(2), and $c$ = 5.599(1) Å. Kahlenberg and Fischer (2000) recently investigated an $Al^{3+}$-substituted $Ca_2Fe_2O_5$ sample with $x$ = 0.126, also belonging to space group *Pnma*. They stated that $Al^{3+}$ is ordered at the tetrahedral site and no $Al^{3+}$ is found at the octahedral position. No further structural studies exist for the *Pnma* phase. Samples with $x$ = 0.57 and 0.72 (Colville and Geller 1972) and brownmillerite $Ca_2AlFeO_5$ (Colville and Geller 1971) itself show *I*2*mb* symmetry. Pure $Ca_2Al_2O_5$, which can only be synthesized at high pressure (Aggarwal et al. 1972), also crystallizes in space group *I*2*mb* (Kahlenberg et al. 2000). The general structural building units are the same, regardless of space group symmetry, and consists of alternating layers of corner sharing $(Fe,Al)O_6$ octahedra and chains of corner-sharing $(Fe,Al)O_4$ tetrahedra running parallel to a. $Ca^{2+}$ is located in the interstitial space between octahedral sheets and layers of single-chain tetrahedra. A representation of the structure of pure $Ca_2Fe_2O_5$ is shown in two different orientations in Figure 1.

Woermann et al. (1968) and Kahlenberg et al. (1997) noticed weak thermal effects in DTA analyses at $T_1$ ≈ 445 °C and $T_2$ ≈ 690 °C in pure $Ca_2Fe_2O_5$. $T_1$ corresponds to the Néel temperature as $Ca_2Fe_2O_5$ is magnetically ordered at room temperature (23 °C), whereas $T_2$ represents a phase transition from *Pnma* to a body-centered cell (Woermann et al. 1968; Kahlenberg et al. 1997). Berastegui et al. (1999) studied the structure of $Ca_2Fe_2O_5$ as a function of temperature up to 1000 °C by means of powder neutron diffraction and found a phase transition from *Pcmn* (a different setting of *Pnma*) to *Icmm* at about 700 °C. For the high-temperature phase the authors preferred the centric space group *Icmm* as it gave slightly better profile agreement indices as compared to the acentric space group *I*2*mb*. However, their data density is low and no information is obtainable as to whether

* E-mail: guenther.redhammer@aon.at

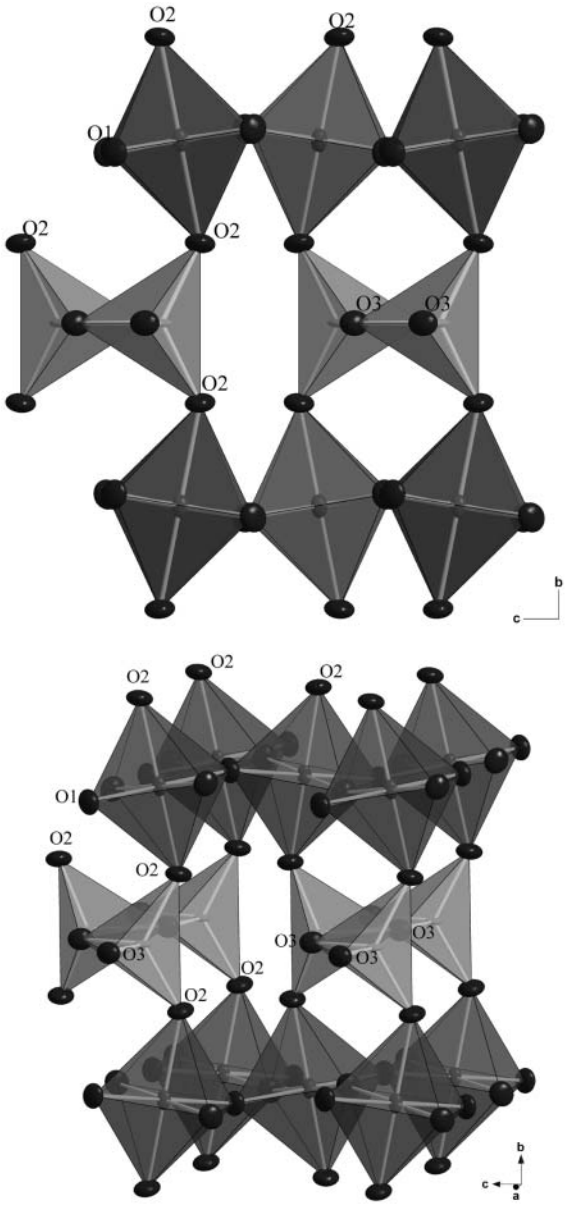


**FIGURE 1.** Plot of the structure of pure $Ca_2Fe_2O_5$ (*Pnma*) $Ca^{2+}$ atoms in the large voids in the structure are deleted for clarity.

there are discontinuities in the lattice parameters associated with the magnetic and the crystallographic phase transition. Very recently Fukuda and Ando (2002) determined the *Pnma-I2mb* phase boundary at high temperature in the $Ca_2Fe_{2-x}Al_xO_5$ system using X-ray powder diffraction. Pure $Ca_2Fe_2O_5$ transforms to *I2mb* at 685 °C; substituting $Al^{3+}$ into $Ca_2Fe_2O_5$ decreases the transformation temperature non-linearly (Fukuda and Ando 2002).

Samples of the $Ca_2(Fe_{2-x}Al_x)O_5$ solid solution series show congruent melting. The melting point of $Ca_2Fe_2O_5$ is ≈1450 °C and is lowered with increasing $Al^{3+}$ content to about 1390 °C for samples with $x = 1.4$ (Newkirk and Thwaitite 1958). Thus single crystals can be prepared by slow cooling of stoichiometric melts (e.g., Smith 1962) or by Czochralski techniques (Colville 1970; Colville and Geller 1971, 1972). Kahlenberg and Fischer (2000) used a flux technique with $CaCl_2$ as a solvent to grow single crystals with $x = 0.126$ at lower temperatures (1200 °C) in order to avoid possible reduction of $Fe^{3+}$ to $Fe^{2+}$, which may take place at temperatures above 1325 °C and atmospheric conditions.

To date all structural investigations of the $Ca_2(Fe_{2-x}Al_x)O_5$ series have been restricted to two compositions of the *Pnma* phase ($x = 0.0$ and 0.126) and three compositions of the body-centered phase ($x = 0.57$, 0.72, and 1.00). No comparative and systematic crystal chemical study of changes in structural parameters with variation of the Al/Fe ratio has been performed before now. The major objective of this study is to provide this crystal chemical information on a finer compositional grid through the compositionally driven *Pnma* → *I2mb* phase transition and to extent it to higher $Al^{3+}$ concentrations. In addition, no description of changes in bond lengths, bond angles, and distortion parameters, associated with the phase transition, is available to date; this information will be given here. In the present study we also re-evaluate the stability field of the *Pnma* phase as a function of temperature and $Al^{3+}$ content and determine the thermal expansion of pure and $Al^{3+}$-substituted $Ca_2Fe_2O_5$ as the stability field given by Fukuda and Ando (2002) seems to be incorrect in some respects.

## EXPERIMENTAL METHODS

### Material synthesis and mineral chemistry

Single crystals were synthesized using both flux growth techniques and slow cooling of melts. Starting materials with the desired stoichiometry were prepared from mechanically homogenized mixtures of $CaCO_3$, $Fe_2O_3$, and $Al_2O_3$. For flux growth experiments, $CaCl_2$ was added as a solvent to the starting material in a ratio of 1:3. A 4 g batch of the mixture (flux and sample) was placed in a platinum crucible with a platinum cover, slowly heated to 1100 °C in a resistance furnace, and held at this temperature for 24 hours in order to homogenize the melt. The temperature was then lowered from 1100 to 900 °C at a rate of 5°/hour. After this the platinum crucible was quenched to room temperature by removing it from the furnace and placing it into a ceramic bowl. Crystals can easily be separated from the solidified flux by hand after the synthesis batch has been subjected to atmospheric (humid) air conditions for a few days leading to a hydrolysis of $CaCl_2$. Dissolving the synthesis batch in water is an alternative method to remove the solidified $CaCl_2$ flux, however, this should be avoided since the brownmillerite phases themselves tend to hydrolyze. Flux growth, as described above, was applied to starting materials with $x = 0.1$, 0.3, 0.6, 0.7, and 1.0 and resulted in prismatic to cuboid, reddish-brown to black crystals with up to 1 mm edge lengths.

Single crystal X-ray diffraction was used to determine the actual amount of $Al^{3+}$ substituted for $Fe^{3+}$ at the octahedral and tetrahedral sites by refining the occupation factor of the specific sites. This is straightforward due to the large difference of the atomic scattering factors for $Fe^{3+}$ and $Al^{3+}$ and has the advantage (over bulk chemical or microprobe analysis) that it yields site-specific compositional information. A somewhat unexpected result occurred upon analyzing the data for crystals grown by the flux method at comparatively low temperatures and slow cooling: single crystals grown from mixtures with $x = 0.3$, 0.6, 0.7, and 1.0 in the starting material showed a final $Al^{3+}$ content of only $x \approx 0.25$ throughout the series. It was not possible to obtain samples with different Fe/Al ratios using the applied flux method (samples with prefix BF...). Thus, in a second synthesis series, starting materials with $x = 0.65$, 0.80, 0.90, and 1.20 were mixed with $CaCl_2$ as a solvent in a ratio of 1:3, placed into covered platinum crucibles and slowly heated to 1200 °C. Instead of slowly cooling the samples, they were isothermally heated at 1200 °C for 7 days and quenched afterward as described above. This procedure again resulted in prismatic to cuboid, reddish-brown to black crystals with edge lengths up to 0.7 mm. Refinement of the actual amount of $Al^{3+}$ substituted for $Fe^{3+}$ in these samples from single crystal X-ray intensity data led to values between $x = 0.53$ and 0.56, larger than before but still without following the nominal $Al^{3+}$

content. We conclude that it is not possible to obtain a continuous Al/Fe solid solution series for $Ca_2(Fe_{2-x}Al_x)O_5$ in the presence of $CaCl_2$; a miscibility gap is proposed to be present. More detailed phase analytical investigations are necessary to clarify the limited $Al^{3+}$ solubility in the presence of $CaCl_2$. This, however, goes beyond the scope of the present study, and will be investigated in a forthcoming paper. It may be noted here that Harchand et al. (1984) report a miscibility gap in the pseudo-binary system CA-CF $[Ca(Al_{2-x}Fe_x)O_4]$ in the range $0.25 < x < 1.66$. The limit for maximum Al-content in C2F ($Ca_2Fe_2O_5$) and in CF ($CaFe_2O_4$) at low temperatures are indeed very similar. However, the results of the present study also suggest that at temperatures at and above 1300 °C this proposed miscibility gap in the $Ca_2(Fe_{2-x}Al_x)O_5$ series is closed.

Due to the fact that it is not possible to obtain a continuous Al/Fe solid solution by growth from a flux, we decided to synthesize samples directly by slow cooling of the melts. For this, the starting material was placed in a small platinum tube (8 mm in length, inner diameter 3 mm), welded tight on one side with the other side left open. Two such tubes were put into a small corundum crucible, placed into a vertical resistance furnace with a platinum wire, and slowly heated to 1500 °C. After 25 hours of homogenization, the temperature was lowered at a rate of 0.5 °C per hour to 1300 °C. The samples were kept at this temperature for another 22–25 hours and were then rapidly quenched by cutting the platinum wire and dropping the sample into a bowl filled with quartz wool and ice water to allow fast cooling and to freeze the Al/Fe distribution at 1300 °C. By this (rather time consuming) method we obtained a further 21 samples with different Al/Fe ratios (samples with prefix BHT...). The shape of the single crystals ranges from thin-platy to cuboid. When thin-platy, a pronounced pleochroism from deep-red to dark brown is observable under the polarization microscope. The single crystals of pure $Ca_2Fe_2O_5$ used in this study were obtained by the ceramic sintering method at 1350 °C (sample with prefix BX000).

The chemical composition of selected $Ca_2(Fe_{2-x}Al_x)O_5$ BHT samples was checked by electron microprobe analysis (JEOL JXA 8600 microprobe, acceleration voltage 15 kV, beam current 30 nA, beam diameter focused to 3 μm). For that purpose crystals were embedded in epoxy resin, polished, covered with carbon and analyzed. At least five analyses from rim to core to rim were measured for each grain and about 20 analyses were performed for each synthesis batch and merged to give the final chemical composition of the sample. The chemical compositions (wt% and structural formula) are reported in Table 1. In all cases the $Al^{3+}$ contents, determined by microprobe analysis, are in excellent agreement with those obtained from the single-crystal structure refinements.

Prior to the single-crystal growth experiments, several samples of $Ca_2(Fe_{2-x}Al_x)O_5$ with $x$ up to 1.34 were prepared as polycrystalline powders by solid-state ceramic sintering techniques at 1300 °C and ambient pressure from stoichiometric mixtures of $CaCO_3$, $Fe_2O_3$, and $Al_2O_3$ in open platinum crucibles. Four cycles of regrinding and re-sintering (for a period of 7 days) were performed in order to guarantee that homogeneous mixed crystals were obtained, even if the desired phases were apparent at the end of the first of the five sintering cycles. The final products are free of additional phases and show sharp Bragg-reflections, which can all be indexed on basis of the brownmillerite metric. The lattice parameters are given in their numeric values as additional material in Deposit Appendix Table 1.[1] The samples produced by ceramic sintering were used for high temperature (H*T*) powder X-ray diffraction experiments. It may be noted here that the H*T* study was done some time before any single crystal work and we had no opportunity to repeat the H*T* measurements with sample material obtained from the single-crystal synthesis experiments described above. As additional material, Deposit Appendix Table 2 lists all the samples used for single crystal X-ray diffraction and Deposit Appendix Table 3 gives the latice parameters for all samples at 25 °C, studied here.

## Mössbauer spectroscopy

To determine the valence state of iron $^{57}$Fe Mössbauer spectra were collected at room temperature with a Mössbauer apparatus in a horizontal arrangement ($^{57}$Co/Rh single-line thin source, constant acceleration, symmetric triangular velocity shape, multi-channel analyzer with 1024 channels, and velocity calibration to α-Fe). For Mössbauer absorber preparation, approximately one half of the melt-grown material was selected, checked under the optical microscopy for purity, carefully ground under ethanol, and analyzed with X-ray powder diffraction to check for phase purity and lattice parameter refinement. After this the sample material was mixed with powdered sugar and placed in Cu rings (inner diameter 10 mm) covered with a high purity Al-foil on one side. The $^{57}$Fe Mössbauer spectra were analyzed with the program suite RECOIL (Rancourt and Ping 1991) in the full static hyperfine interaction Hamiltonian approach using symmetric Lorentzian-shaped subspectra. A complete thickness correction was applied to all data (Rancourt et al. 1993). A detailed temperature-dependent Mössbauer spectroscopic investigation combined with neutron diffraction of the samples is in preparation and will be presented elsewhere.

**TABLE 1.** Chemical composition (wt%) and structural formula of selected samples of the $Ca_2Fe_{2-x}Al_xO_5$ solid-solution series as determined from electron microprobe analyses ($n$ = number of total analyses, numbers in brackets are the estimated standard deviations and refer to the last digit)

| Sample | BHT000 | BHT025 | BHT040 | BHT120n | BHT130 | BHT140 |
|---|---|---|---|---|---|---|
| *n* | 18 | 19 | 19 | 18 | 19 | 18 |
| Weight percent | | | | | | |
| CaO | 41.32 | 42.49 | 43.43 | 46.4 | 47.59 | 48.07 |
| $Fe_2O_3$ | 58.55 | 51.99 | 47.68 | 30.75 | 25.41 | 22.01 |
| $Al_2O_3$ | – | 5.43 | 9.04 | 22.59 | 26.82 | 29.94 |
| sum | 99.87 | 99.91 | 100.15 | 99.78 | 99.83 | 99.91 |
| Sum formula | | | | | | |
| Ca | 2.01(2) | 1.99(1) | 2.01(2) | 2.00(2) | 2.00(2) | 1.99(1) |
| Fe | 2.00(1) | 1.71(2) | 1.55(1) | 0.93(1) | 0.75(2) | 0.64(1) |
| Al | – | 0.28(1) | 0.46(2) | 1.07(2) | 1.24(1) | 1.36(2) |
| O | 5 | 5 | 5 | 5 | 5 | 5 |

## High temperature X-ray powder diffraction

To obtain detailed information on the temperature variation of the lattice parameters and the high temperature phase transition of the *Pnma* phase, step-scan X-ray powder diffraction data were collected on the samples synthesized by ceramic sintering in the temperature range 25–800 °C. The high-temperature measurements were recorded on a Θ-Θ Philips X'Pert diffractometer system, equipped with a PAAR HTK-16 high-temperature chamber, and operated with a Cu X-ray tube. To minimize the temperature gradients within the sample in high-temperature experiments, the finely ground sample material was smeared onto the platinum tape as a thin film. X-ray powder diffraction data were recorded between 10 and 120° 2Θ. For temperatures below 600 °C silicon was used as an internal standard. For $T > 600$ °C silicon cannot be used as internal standard because it reacts with the platinum tape; $Al_2O_3$ was used instead. Lattice parameters were obtained by whole-pattern refinement using the Le Bail method implemented in the program FULLPROF (Rodriguez-Carajal 2001). To check the real temperature of the platinum tape we performed several initial and intermediate test measurements with silicon and corundum (α-$Al_2O_3$) only. For the latter experiments the Bragg reflections of the platinum tape were also clearly observable and thus the unit-cell dimension $a$ of platinum was determinable. From the observed linear variations of the unit-cell parameters we found linear thermal expansion coefficients $\alpha = 4.2–4.4 \times 10^{-6}$/K for pure Si and $\alpha = 9.3–9.6 \times 10^{-6}$/K for platinum in excellent agreement with values given in the literature. For α-$Al_2O_3$ the values are $\alpha = 8.0–8.1 \times 10^{-6}$/K for $a$ and $\alpha = 8.2–8.3 \times 10^{-6}$/K for $c$ in reasonable agreement with the values of Aldebert and Traverse (1984) who gave values of 7.3 and 8.3 × $10^{-6}$/K for $a$ and $c$ respectively.

## Single-crystal structure refinement

Room-temperature single-crystal X-ray diffraction data sets were measured on an imaging-plate diffractometer system (Stoe-IPDS, Mo*K*α radiation, pyrolytic graphite monochromator). Intensity data were collected to 56.5° in 2θ within a φ-range of 0–210°, and the φ increment was 1.5°/ image. The programs X-SHAPE (Stoe and Cie 1996), SHELXS-97 (Sheldrick 1997a), and SHELXL-97 (Sheldrick 1997b) were used for absorption correction, structure solution, and structure refinement respectively. X-ray scattering factors in their ionic form, together with anomalous dispersion coefficients, were taken from the International Tables for Crystallography (Wilson 1992). All lattice parameters were determined from powder X-ray diffraction data (Siemens D500, Cu*K*α radiation, 10–120° 2θ range, secondary graphite monochromator, silicon used as internal standard) and were used in the structure refinement. For this, about one half of the single crystal synthesis batch (BX000, BHT..., and BF... samples) was finely ground under ethanol; some of these samples were subsequently used for $^{57}$Fe Mössbauer spectroscopy.

[1]Deposit Appendix Tables 1 through 3 are available as deposit item AM-04-059 on the American Mineralogist web site at http://www.minsocam.org. Structural data are available both as crystallographic information files (CIFs) and as a file suitable for the program XtalDraw.

## Results and discussion

### Mössbauer spectroscopy

Figures 2a–b display a typical $^{57}$Fe Mössbauer spectrum of a sample of the $Ca_2Fe_{2-x}Al_xO_5$ series ($x = 1.06$) in the non-magnetic state. The spectrum consists of two slightly asymmetric resonance absorption lines. Furthermore, the resonance absorption line at +1.20 mm/s shows a slight shoulder (arrow in Fig. 2b) on the low-velocity side. Although two resonance absorption lines are developed, it is not possible to adequately refine the spectrum with only one doublet. Such a refinement strategy yields statistically unsatisfactorily results ($\chi^2$ values < 4.0) and large misfits are observed, which are most prominent for the +1.20 mm/s absorption line (Fig. 2a). Thus, the two resonance absorption lines correspond to a superposition of two doublets and only a two-doublet model gives acceptable fits. Regardless of the choice of starting parameters, the refinements always converged to the values given in Table 2 within one estimated standard deviation. It is the slight asymmetry of the two absorption lines and the shoulder on the +1.2 mm/s line, which make it possible to find a robust global minimum. The solid curve drawn through the data points is the least-squares fit using two symmetric Lorentzian shaped doublets; the dashed curves represent the two subspectra. Based on the numeric values of the isomer shift δ (Table 2), the low-intensity subspectrum with the smaller δ-value is assigned to high-spin ferric iron at the tetrahedral site and the other to high-spin ferric iron at the octahedral sites. For both sites the quadrupole splitting is among the highest observed for $Fe^{3+}$. This is indicative of a distinctly asymmetric charge distribution around the probe nucleus resulting from a distorted (elongated) local geometry around the $Fe^{3+}$ ion at the corresponding octahedral and tetrahedral sites respectively. The quadrupole splitting increases somewhat with increasing $Al^{3+}$ content. This is an indication of an increasing distortion of the O-atom coordination around ferric iron with increasing $Al^{3+}_{tot}$. Most important for the purpose of the present paper is the absence of any signs indicative of ferrous iron. This means that during single crystal growth from the melt at high temperatures (1500 °C to 1300 °C) no reduction of ferric to ferrous iron has taken place.

Pure $Ca_2Fe_2O_5$ and samples up to $x \approx 1.0$ (Geller et al. 1971; Redhammer unpublished results) are (antiferro) magnetically ordered at room temperature. At temperatures below $T_N$, both magnetic dipole and electric quadrupole interactions occur simultaneously. This allows six transitions between the exited and the ground state of the $^{57}$Fe probe nucleus and results in a magnetically split 6-line spectrum (instead of a doublet when only electric quadrupole interactions occur). The $^{57}$Fe Mössbauer spectrum at 25 °C for pure $Ca_2Fe_2O_5$ is shown in Figure 2c. The magnetically split spectra of the $Ca_2Fe_{2-x}Al_xO_5$ series are complex to evaluate, especially when $Fe^{3+}$ is partly substituted by $Al^{3+}$. Due to the different environments, additional lines appear and line broadening takes place. A subsequent paper will deal with the $^{57}$Fe Mössbauer spectra of the $Ca_2Fe_{2-x}Al_xO_5$ series in detail and we will concentrate on pure $Ca_2Fe_2O_5$ alone. For this composition, the room-temperature Mössbauer spectrum could be satisfactorily evaluated by making use of two magnetically split 6-line subspectra (Fig. 2c) for high-spin ferric iron at the octahedral and the tetrahedral sites respectively. The point sym-

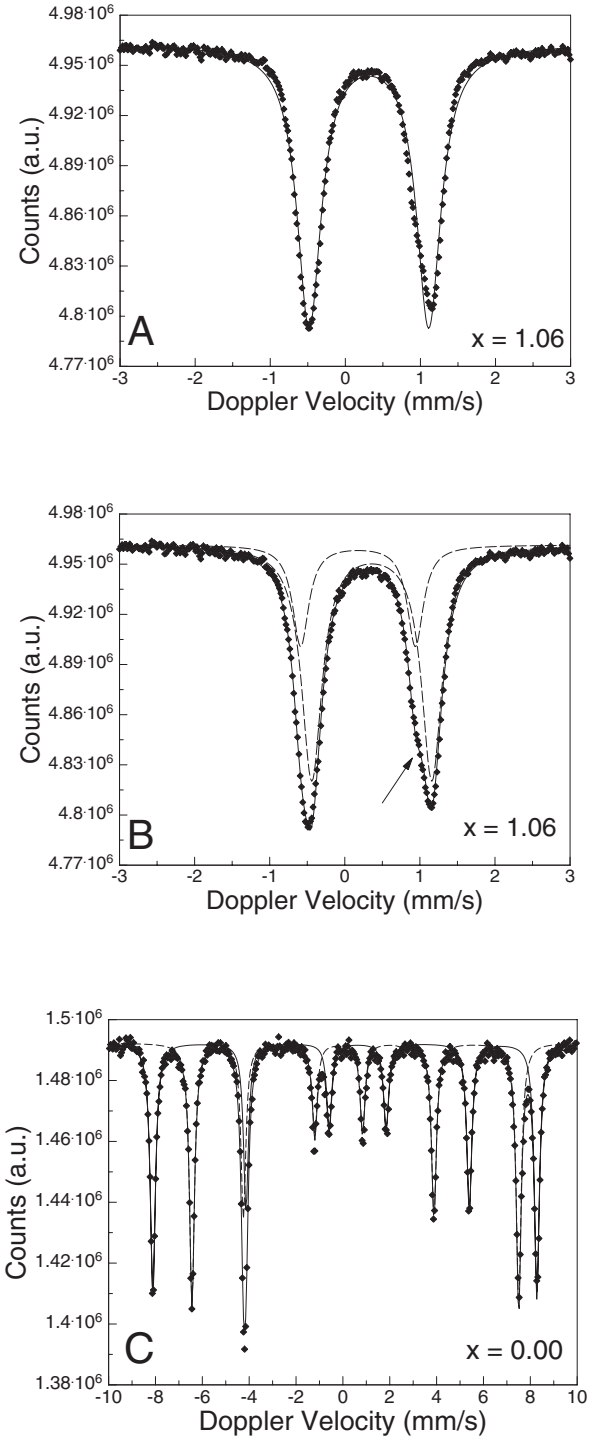


**Figure 2.** $^{57}$Fe Mössbauer spectrum of (**a**) sample $Ca_2Fe_{0.64}Al_{1.36}O_5$ and (**b**) of pure $Ca_2Fe_2O_5$, both spectra recorded at 25 °C. The solid diamonds are the experimental data and the solid curves shown through the data points are the least squares fit with symmetric Lorentzian shaped doublets (dashed curves).

**TABLE 2.** $^{57}$Fe Mössbauer hyperfine parameters for selected samples of the $Ca_2Fe_{2-x}Al_xO_5$ solid-solution series, collected at 25 °C

| Sample | *x* | δ (mm/s) | Δ (mm/s) | Γ (mm/s) | $H_0$ (T) | θ (deg.) | η | A (%) | $Fe^{3+}$ apfu | site |
|---|---|---|---|---|---|---|---|---|---|---|
| BHT 140 | 1.36 | 0.187(3) | 1.591(7) | 0.126(6) | – | – | – | 22.3(4) | 0.144(7) | $Fe^{3+}$ (tet.) |
| | | 0.368(3) | 1.625(6) | 0.158(3) | – | – | – | 77.7(5) | 0.500(7) | $Fe^{3+}$ (oct.) |
| BHT 130 | 1.26 | 0.182(3) | 1.565(6) | 0.125(3) | – | – | – | 22.4(5) | 0.166(8) | $Fe^{3+}$ (tet.) |
| | | 0.363(4) | 1.616(4) | 0.159(3) | – | – | – | 77.6(5) | 0.575(8) | $Fe^{3+}$ (oct.) |
| BHT 120n | 1.08 | 0.176(3) | 1.527(6) | 0.131(2) | – | – | – | 25.5(6) | 0.235(11) | $Fe^{3+}$ (tet.) |
| | | 0.360(2) | 1.599(3) | 0.165(2) | – | – | – | 74.5(5) | 0.687(11) | $Fe^{3+}$ (oct.) |
| BHT 110n | 0.97 | 0.179(2) | 1.526(4) | 0.138(2) | – | – | – | 27.5(4) | 0.279(8) | $Fe^{3+}$ (tet.) |
| | | 0.364(3) | 1.591(3) | 0.175(3) | – | – | – | 72.5(5) | 0.735(8) | $Fe^{3+}$ (oct.) |
| BX000 | 0.00 | 0.176(1) | −1.471(5) | 0.127(3) | 42.81(2) | 90 | 0.01(1) | 50.6(4) | 1.01(3) | $Fe^{3+}$ (tet.) |
| | | 0.357(2) | 1.514(4) | 0.130(3) | 50.35(1) | 85.1(2) | 0.23(1) | 49.4(5) | 0.99(4) | $Fe^{3+}$ (oct.) |

*Notes:* δ = isomer shift, Δ = quadrupole splitting, Γ = half width at full maximum, $H_0$ = internal magnetic field at the probe nucleus, θ = polar angle between $H_0$ and $V_{zz}$ (main component of the electric field gradient), η = asymmetry parameter $(V_{xx} - V_{yy})/V_{zz}$.

metry of the octahedral and tetrahedral $Fe^{3+}$ sites are $\bar{1}$ and *m* respectively. Thus the electric field gradient (efg) at the octahedral site has no symmetry restrictions, whereas for the tetrahedral site one principal axis has to be perpendicular to the mirror a-c plane, thus restricting the other two efg axes to the a-c plane. The $^{57}$Fe hyperfine parameters for $Fe^{3+}$ in $Ca_2Fe_2O_5$ below $T_N$ are also given in Table 2. The asymmetry parameter η is small for both sites meaning that the efg has axial symmetry for the tetrahedral ($\eta = 0$; $V_{xx} = V_{yy}$) and nearly axial symmetry for the octahedral site. The angle θ between the main component of the efg, $V_{zz}$, and the magnetic field at the nucleus, $H_0$, is 90° within experimental error for the tetrahedral and 85° for the octahedral site. This implies that $V_{zz}$ is oriented in or near *a* plane perpendicular to $H_0$. As the easy direction of magnetization is parallel to the *a* axis in *Pnma* symmetry (Geller et al. 1971), the main efg component $V_{zz}$ is nearly parallel to the *b* axis for the octahedral and ∥ to *b* for the tetrahedral site.

### X-ray powder diffraction

Fukuda and Ando (2002) recently determined the temperature-composition (*T*-*x*) stability of the *Pnma* phase of the $Ca_2Fe_{2-x}Al_xO_5$ solid solution series and the thermal evolution of the lattice parameters of pure $Ca_2Fe_2O_5$. Independent of this work, we have determined the boundary of the *Pnma* phase as a function of *T* and *x* and studied the thermal expansion of selected samples along the $Ca_2Fe_{2-x}Al_xO_5$ series ($x$ = 0.0, 0.40, 0.50, 0.55, 0.70, and 1.00) in more detail. The Bragg reflection (1 3 1), appearing between 29 and 30° 2θ in the *Pnma* phase with Cu radiation, depending on *T* and *x*, can be used to detect the phase transition from *Pnma* to a body-centered cell at high temperature. Figure 3a shows a sector of the X-ray powder diffraction pattern displaying the temperature-dependent decay of the intensity of (1 3 1) in $Ca_2Fe_2O_5$. The X-ray powder diffraction pattern above the phase transition can be refined in space group *I*2*mb* or *Immb*, but the former yields better profile agreement indices.

Along with the disappearance of the $h + k + l = 2n + 1$ reflections, e.g., (1 3 1), some weak and broad extra reflections appear in the 2θ region between 15° and 30°, namely at 18.9°, 19.8°, 20.8°, 26.1°, and 27.8° (Fig. 3a). These reflections could not be indexed on the basis of orthorhombic symmetry and using the cell parameters obtained from the main reflections of the body-centered phase. However, we can rule out that these reflections are due to an impurity phase or exsolution effects, as the reflections disappear when the temperature is lowered to the region where the *Pnma* phase is stable (Fig. 3a). The appearance of these extra reflections in the high temperature phase was not

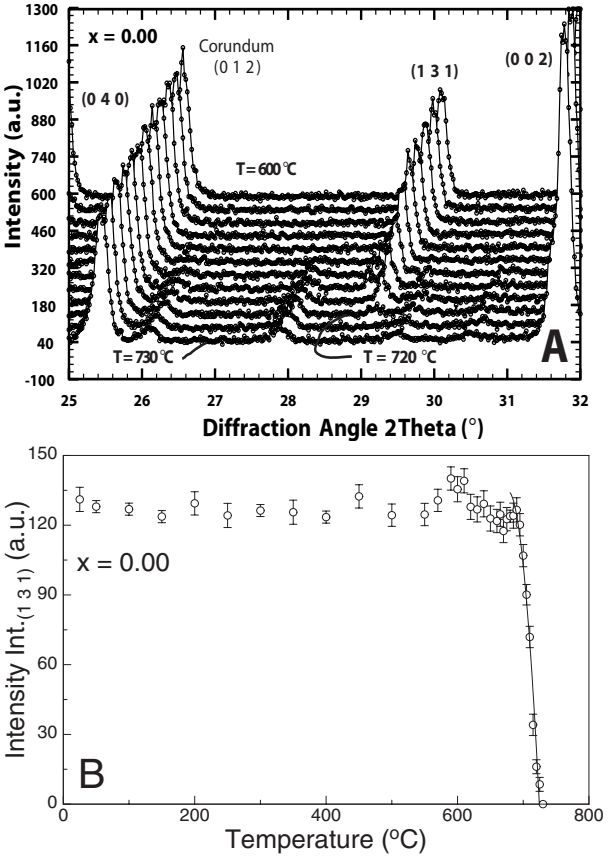


**FIGURE 3.** (**a**) Section of the powder X-ray diffraction pattern of pure $Ca_2Fe_2O_5$ showing the decay of intensity of the (1 3 1) reflection upon heating for the temperature region 600 °C to 730 °C. Note the disappearance of the reflection between 720 and 725 °C. (**b**) Numerical values for the temperature-dependent variation of the integral intensity of the (1 3 1) reflection.

mentioned in literature so far. Their presence might be seen as an indication for an incommensurate modulation of the high temperature structure of $Ca_2Fe_2O_5$ above 725 °C. X-ray diffraction on single crystals is necessary to clarify for this. The symmetry and structure of the high-temperature phase remains an unsettled issue. In what follows, we will assume *I*2*mb* symmetry—put in quotations—for the high-temperature phase to indicate that the space group might be wrong. For the following it should be noted further, that this uncertainty in space group assignment only accounts for the powder X-ray diffraction experiments in the high temperature phase, not for the measurements at 25

°C, both in the powder and the single crystal X-ray diffraction experiments. Close to the phase boundary, the intensity of (1 3 1) rapidly drops to zero and completely disappears (Fig. 3b) at the phase transition ($T_p$). The *Pnma*-"*I2mb*" transition takes place at 724 ± 4 °C in $Ca_2Fe_2O_5$, is completely reversible, and shows no hysteresis behavior within experimental error. All extra reflections observed in the high temperature "*I2mb*" phase completely disappear The transition temperature in our study is slightly higher than the one found by Fukuda and Ando (2002), Kahlenberg et al. (1997), and Woermann et al. (1968), who proposed a transition temperature of ≈690 °C.

In contrast to the findings of Fukuda and Ando (2002) we found a linear decrease of $T_p$ with increasing $Al^{3+}$ content (Table 3[2], Fig. 4) with a sudden drop of the transition temperature above $x = 0.65$. At room temperature the composition-dependent change from *Pnma* to *I2mb* symmetry takes place between $x = 0.65$ and 0.70. In the latter sample, no indications of a (1 3 1) reflection were present. Also, no extra reflections, which would be similar to those of the high-temperature phase, could be detected. For $x = 0.65$ a weak (1 3 1) reflection was detectable. For this latter composition, the high temperature X-ray diffraction measurements revealed a transition temperature of 623 ± 5 °C. According to our results, a substitution of 0.1 $Al^{3+}$ per formula unit lowers the phase transition temperature linearly by ≈15 °C. Woermann et al. (1968) determined the phase boundary of the *Pnma*-"*I2mb*" transition for samples of the $Ca_2Fe_{2-x}Al_xO_5$ series with different $x$ from DTA signals. For $x = 0.6$ they found a transition temperature of ≈630 °C. A slight increase of the $Al^{3+}$ content stabilizes the body-centered cell and samples with $x > 0.6$ have *I2mb* symmetry at 25 °C (Woermann et al. 1968). Smith (1962) found that the phase transition occurs at $Al^{3+}$ contents of $x = 0.66$ at 25 °C which is in good agreement with our findings.

Deposit Figures 5a–d[3] depict the temperature dependence of the unit-cell parameters for pure $Ca_2Fe_2O_5$. For *a*, *b* and *c*, as well as for *V*, there is a linear increase of the unit-cell lengths with temperature up to ≈420 °C. At this temperature there is a discontinuity in the temperature variations. Beyond that the increase of lattice parameters exhibits a slightly greater slope than below 420 °C. Between ≈480 and 700 °C lattice parameters again vary linearly with temperature, and at ≈720 °C a second discontinuity appears, which is most pronounced for the *c* lattice parameter. The unit-cell volume exhibits both discontinuities in a very distinct way (deposit Fig. 5d). The first kink in the temperature variation of lattice parameters can be correlated with the magnetic phase transition of $Ca_2Fe_2O_5$, which was found to take place at 440 °C (Geller et al. 1971), whereas the second kink is associated with the *Pnma*-"*I2mb*" phase transition. All

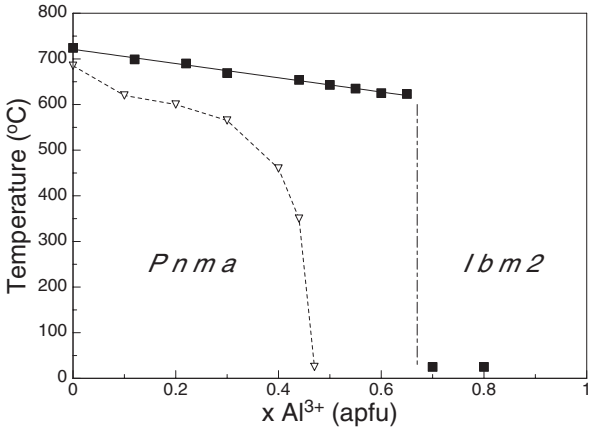


**FIGURE 4.** Stability region of the *Pnma* phase in the $Ca_2Fe_{2-x}Al_xO_5$ solid-solution series. Filled squares are data from this study and open triangles are the data from Fukuda and Ando (2002). A linear regression line is fitted to the data of this study for ($0 \le x \le 0.65$) and serves as a guide to the eye.

the other samples, investigated by H*T* X-ray diffraction, show a linear variation of lattice parameters with temperature. As an example, the temperature variation for $Ca_2FeAlO_5$ ($x = 1.0$) is shown in deposit Figure 6[3].

We have determined the linear thermal expansion coefficient α, which is given by the formula:

$$\alpha = (l_T - l_0)/(l_0 * [T - T_0])$$

where $l_T$ is the unit-cell length at temperature $T$, $l_0$ is the length at $T_0$ = 25 °C, from the data between 25–420 °C (*Pnma*-phase beyond the magnetic phase transition) and above 720 °C ("*I2mb*" phase), The linear thermal expansion of $Ca_2Fe_2O_5$ was found to be quite anisotropic with the highest value along the b axis ($\alpha = 23.1 \times 10^{-6}$/K), whereas along *a* and *c* the linear thermal expansion is nearly one-third of the value along *b*, namely $8.8 \times 10^{-6}$/K and $9.3 \times 10^{-6}$/K, respectively. For the "*I2mb*" phase (720–800 °C) slightly different values were found (Table 4[2]). It is the *b*-direction, in which octahedral and tetrahedral layers are stacked up and in which M-$O_{apex}$ bonds (M = octahedral cation) are pointing (Fig. 1). The large thermal expansion along [0 1 0] may be interpreted in as much as that the tilting of the octahedral layer may decreases towards high temperatures and that M-$O_{apex}$ bonds expand more rapidly with temperature than the M-O bonds in the equatorial-plane of the octahedra. The thermal expansion along the *a*-axis, intermediate between the one of *b* and *c*, probably is controlled by the expansion of the octahedral site and the changes within the O3-O3-O3 tetrahedral bridging angle, which should change distinctly upon heating. Changes in the tilt of the octahedra will also require changes in the O3-O3-O3 angle. The small thermal expansion along the *c*-axis is proposed to be controlled by the expansion of the tetrahedral site, which—normally—acts as a very rigid unit and does not show large alterations in bond lengths and bond angles upon heating. The linear thermal expansion shows some variations with composition. Between $x = 0.0$ and 0.55 it decreases non-linearly with increasing $Al^{3+}$ content by ≈18% and ≈48% for *b* and *c* respectively, whereas the linear

[2]For a copy of Tables 3, 4, 7, and 8, document item AM-04-057, contact the Business Office of the Mineralogical Society of America (see inside front over of recent issue) for price information. Deposit items may also be available on the American Mineralogist web site at http://www.minsocam.org.

[3]For a copy of Figures 5, 6, 10, 11, and 13, document item AM-04-058, contact the Business Office of the Mineralogical Society of America (see inside front over of recent issue) for price information. Deposit items may also be available on the American Mineralogist web site at http://www.minsocam.org.

expansion coefficient along *a* increases by ≈20% (Fig. 7, Table 4[2]). The thermal expansion of compositions having *I2mb* symmetry is different from the *Pnma* phase. A break in the trend of the data points is observable at the phase transition in Figure 7. Extrapolation of data for samples with *I2mb* symmetry at 25 °C to pure $Ca_2Fe_2O_5$ in the "*I2mb*" symmetry (data between 720 and 800 °C), yields exactly these values measured for $Ca_2Fe_2O_5$ for lattice parameters *b* and *c*.

### Single crystal structure refinements of $Ca_2Fe_{2-x}Al_xO_5$ compounds

From the single crystal X-ray diffraction experiments the change from the primitive to the body-centered cell takes place at $x = 0.56$ at 25 °C along the $Ca_2Fe_{2-x}Al_xO_5$ binary join. This is different from the transition composition found in X-ray powder diffraction experiments discussed in the previous section but agrees very well with the findings of Colville and Geller (1971) for samples, grown by the Czrochalski method. They also found a transition composition of $x = 0.56$. The difference in transition composition may very well be due to the different methods of sample preparation. Analysis of the systematic absences supports the assignment of the centric space group *Pnma* for all samples with $x < 0.56$. For samples with $x > 0.56$, systematic absences suggested the acentric space group *I2mb*. Intensity statistics yielded $|E^2 - 1| = 0.764–0.798$, close to the expected value of 0.736 for non-centrosymmetric structures. $|E^2 - 1|$ steadily increases with increasing $Al^{3+}$ content. For $x < 0.56$ intensity statistics yield values of $|E^2 - 1| = 0.923–0.935$, and the change of $|E^2 - 1|$ at the phase transition is very pronounced (Table 5). Experimental details, crystallographic, and refinement parameters of selected samples are given in Table 5, atomic coordinates and equivalent isotropic displacement factors can be found in Table 6, the anisotropic atomic displacement parameters are compiled in deposit Table 7[2], and selected interatomic distances and angles as well as selected polyhedral distortion parameters are given in deposit Table 8[2]. Additional structure refinements with anisotropic atomic displacement parameters in *Pnma* and *I2mb* respectively converged to final $R_1$ (all data) values below 4.1% and final w$R_2$ (all data) values below 6.7% (data sets corrected for absorption effects). These maximum values hold true for all compositions studied here, not only to the selection given in Tables 5 through 8. Refinements using the centrosymmetric space group *Immb* for samples with $x > 0.56$ did not converge to w$R_2$—values below 35% and no plausible structure models were found.

The equivalent isotropic ($U_{eq.}$) as well as the anisotropic displacement parameters ($U_{ij}$) did not show a systematic variation with the chemical composition of the samples. At best, there may be a slight increase of $U_{eq}$ with increasing $Al^{3+}_{tot}$. The M (octahedral) and T (tetrahedral) cations have the smallest $U_{eq}$ values (0.003–0.006 Å). Calcium and the O1 and O3 atoms have similar $U_{eq}$ values (0.006–0.009 Å). The largest equivalent isotropic displacements (0.009–0.012 Å) are observed for the O2 atom, which links the octahedral with the tetrahedral sheet.

**Lattice parameters.** The lattice parameters of the $Ca_2Fe_{2-x}Al_xO_5$ solid-solution series decrease with increasing substitution of the smaller $Al^{3+}$ for the larger $Fe^{3+}$ ion. The plot of the *a* unit-cell parameter vs. $Al^{3+}$ content (Fig. 8a) is a straight line up to $x = 0.56$, and the same is true for the *b* unit-cell parameter

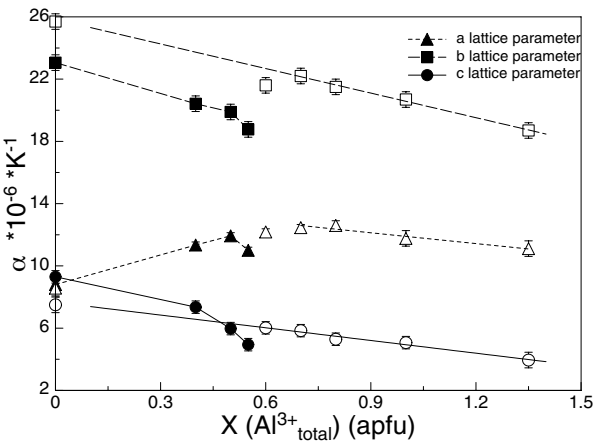


**FIGURE 7.** Linear thermal expansion coefficient α for different samples of the $Ca_2Fe_{2-x}Al_xO_5$ solid-solution series, determined from the temperature evolution of unit-cell parameters. Filled and open symbols correspond to samples with *Pnma*and *I2mb* symmetry, respectively.

(Fig. 8b). The *c* parameter (Fig. 8c) shows only a small, but slightly non-linear decrease with increasing $Al^{3+}$. At $x \approx 0.56$ discontinuities appear in all three directions, *a*, *b*, and *c*, and in the unit-cell volume (Fig. 8d). Above this discontinuity point, *a* again decreases linearly, however with different (greater) slope. The *b* unit-cell parameter exhibits a non-linear behavior, which is evident at high $Al^{3+}$ concentrations. The slight jump in lattice parameters upon the transition from the primitive to the body-centered cell and the larger decrease of lattice parameters with increasing $Fe^{3+}$ by $Al^{3+}$ substitution is most evident for the *c* parameter. Literature data, displayed in Figure 8 for comparison, agree with our data for low $Al^{3+}$ contents. For $x > 0.6$ there is some diversity in the literature and no smooth trends are visible. Our data, however, give rise to smooth variations with compositions, which go beyond what can be learned from the literature. This especially accounts for the slight jump in lattice parameters at the phase transition composition and the course of data at high $Al^{3+}_{tot}$ concentrations. Lattice parameters of the samples synthesized by ceramic sintering at 1300 °C are included in Figure 8 and fit the data trend for the samples synthesized as single crystals. The numeric values of all these lattice parameters can be found in Deposit Appendix Table 1.[1]

**Octahedral site.** There are two groups of M-O bond lengths within the $(Fe^{3+}, Al^{3+})O_6$ site. In $Ca_2Fe_2O_5$ four out of the six M-O bonds lie in the range 1.961(2)–1.969(2) Å, whereas the other two have lengths of 2.121(2) Å. The latter two equivalent bond distances are those to the O2 atom bridging the octahedral sheet with the tetrahedral chains along *b* axis. Thus the octahedra appear to be elongated along [0 1 0]. Substituting the smaller $Al^{3+}$ cation ($r^{VI} = 0.530$ Å, Shannon and Prewitt 1969) for the larger $Fe^{3+}$ cation ($r^{VI} = 0.645$ Å, Shannon and Prewitt 1969) linearly decreases the average M-O distance (Fig. 9a). After the phase transition, there again is a linear decrease of <M-O> vs. $Al^{3+}_{tot}$, however with a larger negative slope, suggesting that more $Al^{3+}$ enters the octahedral site. The M-O1 bond lengths (Fig. 9b),

**TABLE 5.** Experimental details for the X-ray data collection and crystallographic and refinement parameters of selected samples of the $Ca_2Fe_{2-x}Al_xO_5$ solid solution series

| | BX000_1 | BHT005_2 | BHT015_1 | BHT025_2 | BHT030_3 | BHT035_1 | BHT040_2 | bf80i_1 | BHT55_1 |
|---|---|---|---|---|---|---|---|---|---|
| Crystal data | | | | | | | | | |
| $x$ $Al^{3+}_{tot}$ | 0.000 | 0.115 | 0.204 | 0.276 | 0.365 | 0.408 | 0.441 | 0.559 | 0.552 |
| Space group | *Pnma* | *Pnma* | *Pnma* | *Pnma* | *Pnma* | *Pnma* | *Pnma* | *Pnma* | *I2mb* |
| $a$ (Å) | 5.4268(3) | 5.4217(3) | 5.4140(2) | 5.4071(3) | 5.4027(4) | 5.3986(3) | 5.3936(3) | 5.3876(2) | 5.3808(3) |
| $b$ (Å) | 14.7631(5) | 14.7432(6) | 14.7163(5) | 14.6949(8) | 14.6779(9) | 14.6631(7) | 14.6476(7) | 14.6302(6) | 14.6131(8) |
| $c$ (Å) | 5.5969(2) | 5.5960(3) | 5.5947(2) | 5.5941(3) | 5.5923(4) | 5.5910(2) | 5.5899(3) | 5.5877(3) | 5.5911 |
| $V$ (Å$^3$) | 448.40 | 447.3 | 445.75 | 444.49 | 443.47 | 442.59 | 441.62 | 440.43 | 439.63 |
| $M_r$ | 271.9 | 268.55 | 265.97 | 263.89 | 261.32 | 260.08 | 259.13 | 255.72 | 255.92 |
| $D_{calc}$ (g/cm$^3$) | 4.03 | 3.99 | 3.963 | 3.943 | 3.914 | 3.903 | 3.897 | 3.857 | 3.867 |
| μ (mm$^{-1}$) | 8.67 | 8.36 | 8.13 | 7.94 | 7.696 | 7.584 | 7.504 | 7.174 | 7.208 |
| Color | black | black | black | black | black | black | black | black | black |
| shape | cuboid | cuboid | prismatic | prismatic | cuboid | cuboid | platy | cuboid | platy |
| size max. (mm) | 0.08 | 0.22 | 0.18 | 0.23 | 0.19 | 0.17 | 0.21 | 0.28 | 0.19 |
| Data collection | | | | | | | | | |
| 2θ max (°) | 56.29 | 56.32 | 56.22 | 56.16 | 56.49 | 56.22 | 56.18 | 56.29 | 55.96 |
| $h$ $k$ $l$ range: $h$ | −7 → 6 | −7 → 7 | −7 → 7 | −7 → 6 | −7 → 6 | −6 → 6 | −6 → 7 | −6 → 6 | −7 → 7 |
| $k$ | −19 → 19 | −19 → 19 | −19 → 19 | −18 → 19 | −17 → 19 | −19 → 19 | −18 → 19 | −19 → 19 | −18 → 19 |
| $l$ | −7 → 7 | −7 → 7 | −7 → 7 | −7 → 7 | −7 → 7 | −7 → 7 | −7 → 7 | −7 → 7 | −6 → 6 |
| $T_{min.}$ | 0.522 | 0.192 | 0.283 | 0.259 | 0.207 | 0.251 | 0.381 | 0.102 | 0.481 |
| $T_{max.}$ | 0.591 | 0.314 | 0.409 | 0.386 | 0.278 | 0.354 | 0.500 | 0.181 | 0.607 |
| $N_{measured}$ | 4018 | 3894 | 4052 | 3575 | 3582 | 3880 | 3829 | 3910 | 2098 |
| $N_{independent}$ | 568 | 558 | 563 | 561 | 559 | 548 | 552 | 548 | 506 |
| $R_{int}$ (%) | 4.55 | 3.61 | 3.53 | 5.70 | 4.09 | 3.30 | 3.13 | 3.49 | 2.72 |
| $\lvert E^2 - 1 \rvert$ | 0.923 | 0.928 | 0.930 | 0.930 | 0.937 | 0.935 | 0.938 | 0.932 | 0.775 |
| Refinement | | | | | | | | | |
| $N_{parameters}$ | 47 | 51 | 51 | 51 | 51 | 51 | 51 | 51 | 50 |
| $R_1 > 4s$ (%) | 2.15 | 1.64 | 2.12 | 2.18 | 1.99 | 1.53 | 1.90 | 2.25 | 1.68 |
| $R_1$ all (%) | 3.28 | 1.84 | 2.29 | 4.11 | 2.84 | 1.84 | 2.13 | 2.64 | 1.76 |
| $wR_2 > 4\sigma$ (%) | 4.97 | 3.96 | 5.22 | 4.13 | 4.38 | 3.58 | 5.03 | 5.44 | 4.30 |
| $wR_2$ all (%) | 6.71 | 4.40 | 5.72 | 5.05 | 4.71 | 4.04 | 5.45 | 6.64 | 4.43 |
| G.O.F | 1.350 | 1.252 | 1.282 | 1.110 | 1.050 | 1.126 | 1.177 | 1.322 | 1.181 |
| $\Delta\rho_{min}$ (e/Å$^3$) | −0.60 | −0.45 | −0.65 | −0.64 | 0.61 | −0.35 | −0.36 | −0.53 | −0.57 |
| $\Delta\rho_{max}$ (e/Å$^3$) | 0.61 | 0.44 | 0.52 | 0.50 | 0.58 | 0.35 | 0.67 | 0.68 | 0.47 |
| weight $w$ ($a$, $b$) | 0.0317 | 0.0248 | 0.0351 | 0.0194 | 0.0269 | 0.0253 | 0.0364 | 0.0269 | 0.0316 |
| | | 0.142 | 0.124 | | | | 0.088 | 0.840 | 0.080 |
| Extinction $k$ | 0.0205 | 0.0254 | 0.0344 | 0.0240 | 0.0192 | 0.0181 | 0.0039 | 0.0236 | 0.0006 |

*Notes:* $w = 1/[\sigma^2(F_O^2) + (aP)^2 + bP]$ where $P = (F_O^2 + 2F_C^2)/3$; $= k[1 + 0.001*F_C^2 l3/\sin(2Q)]^{-1/4}$. All measurements performed at 25(2) °C with a STOE IPDS I diffractometer (scan type = rotation method) Mo*K*α radiation [λ = 0.71073 (Å)]; absorption correction via equivalents ($T_{min}$, $T_{max}$ = minimum and maximum transmission). Lattice parameters given are obtained from whole pattern refinement of X–ray powder data of the corresponding synthesis batch; $Z = 4$ for all samples.

**TABLE 6.** Atomic co-ordinates and equivalent isotropic displacement parameters of selected samples of the $Ca_2Fe_{2-x}Al_xO_5$ solid-solution series

| | | BX000_1 | BHT005_2 | BHT015_1 | BHT025_2 | BHT030_3 | BHT035_1 | BHT040_2 | bf80i_2 | BHT55_1 |
|---|---|---|---|---|---|---|---|---|---|---|
| Ca | $x$ | 0.4808(1) | 0.48141(6) | 0.48243(7) | 0.4832(1) | 0.48378(8) | 0.48454(6) | 0.48477(7) | 0.48559(9) | 0.49099(8) |
| | $y$ | 0.10798(4) | 0.10802(3) | 0.10813(3) | 0.10819(4) | 0.10821(3) | 0.10834(2) | 0.10835(3) | 0.10864(4) | 0.10817(3) |
| | $z$ | 0.0227(1) | 0.02331(6) | 0.02388(7) | 0.02402(9) | 0.02456(8) | 0.02498(5) | 0.02493(7) | 0.02569(8) | 0.02643(9) |
| | $U_{eq}$ | 0.0073(2) | 0.0065(1) | 0.0068(2) | 0.0074(2) | 0.0089(2) | 0.0079(1) | 0.0077(2) | 0.0081(2) | 0.0064(2) |
| M-site | $x$ | 0 | 0 | 0 | 0 | 0 | 0 | 0 | 0 | 0.00101(9) |
| | $y$ | 0 | 0 | 0 | 0 | 0 | 0 | 0 | 0 | 0 |
| | $z$ | 0 | 0 | 0 | 0 | 0 | 0 | 0 | 0 | 0 |
| | $U_{eq}$ | 0.0049(2) | 0.0033(1) | 0.0036(2) | 0.0050(2) | 0.0060(2) | 0.0048(1) | 0.0048(2) | 0.0048(2) | 0.0032(2) |
| | Occ. Fe | 1.00 | 0.966(7) | 0.952(5) | 0.964(5) | 0.932(6) | 0.906(5) | 0.920(6) | 0.880(5) | 0.862(5) |
| | Occ. Al | 0.00 | 0.034(7) | 0.048(5) | 0.036(5) | 0.068(6) | 0.094(5) | 0.080(6) | 0.120(5) | 0.138(5) |
| T-site | $x$ | 0.9461(1) | 0.94628(6) | 0.94682(7) | 0.9472(1) | 0.94757(9) | 0.94803(7) | 0.94805(8) | 0.9490(1) | 0.9526(1) |
| | $y$ | 1/4 | 1/4 | 1/4 | 1/4 | 1/4 | 1/4 | 1/4 | 1/4 | 1/4 |
| | $z$ | 0.93403(9) | 0.93351(6) | 0.93280(7) | 0.9325(1) | 0.93200(9) | 0.93142(6) | 0.93132(7) | 0.9308(1) | 0.9299(1) |
| | $U_{eq}$ | 0.0046(2) | 0.0026(1) | 0.0032(2) | 0.0031(2) | 0.0046(2) | 0.0041(1) | 0.0038(2) | 0.0049(2) | 0.0027(2) |
| | Occ. Fe | 1.00 | 0.920(8) | 0.844(5) | 0.760(5) | 0.703(6) | 0.686(5) | 0.639(4) | 0.660(5) | 0.586(6) |
| | Occ. Al | 0.00 | 0.080(8) | 0.156(5) | 0.240(5) | 0.297(6) | 0.314(5) | 0.361(4) | 0.440(5) | 0.414(6) |
| O1 | $x$ | 0.2628(3) | 0.2622(2) | 0.2610(2) | 0.2604(3) | 0.2596(3) | 0.2589(2) | 0.2589(2) | 0.2579(3) | 0.2500(3) |
| | $y$ | 0.9843(1) | 0.98432(8) | 0.98458(9) | 0.9847(1) | 0.9849(1) | 0.98498(7) | 0.98509(9) | 0.9852(1) | 0.9858(9) |
| | $z$ | 0.2370(3) | 0.2375(2) | 0.2386(2) | 0.2394(3) | 0.2404(3) | 0.2412(2) | 0.2411(2) | 0.2423(3) | 0.2532(3) |
| | $U_{eq}$ | 0.0070(4) | 0.0062(2) | 0.0063(3) | 0.0062(4) | 0.0084(3) | 0.0077(2) | 0.0078(3) | 0.0080(4) | 0.0061(2) |
| O2 | $x$ | 0.0240(3) | 0.0236(2) | 0.0232(2) | 0.0223(3) | 0.0227(3) | 0.0220(2) | 0.0215(2) | 0.0206(3) | 0.0247(3) |
| | $y$ | 0.1406(1) | 0.14090(9) | 0.1416(1) | 0.1415(1) | 0.1419(1) | 0.14226(8) | 0.1422(1) | 0.1427(1) | 0.1427(1) |
| | $z$ | 0.0735(3) | 0.0723(2) | 0.0719(2) | 0.0719(4) | 0.0719(3) | 0.0713(2) | 0.0713(2) | 0.0707(3) | 0.0699(3) |
| | $U_{eq}$ | 0.0087(4) | 0.0082(3) | 0.0087(3) | 0.0092(4) | 0.0109(3) | 0.0101(3) | 0.0101(3) | 0.0101(4) | 0.0089(4) |
| O3 | $x$ | 0.5991(5) | 0.5992(3) | 0.6007(3) | 0.6026(4) | 0.6034(4) | 0.6045(3) | 0.6052(3) | 0.6056(5) | 0.6097(4) |
| | $y$ | 1/4 | 1/4 | 1/4 | 1/4 | 1/4 | 1/4 | 1/4 | 1/4 | 1/4 |
| | $z$ | 0.8741(4) | 0.8736(3) | 0.8720(3) | 0.8711(5) | 0.8698(4) | 0.8687(2) | 0.8686(3) | 0.8683(4) | 0.8685(5) |
| | $U_{eq}$ | 0.0074(5) | 0.0063(3) | 0.0070(3) | 0.0072(6) | 0.0099(5) | 0.0088(3) | 0.0087(4) | 0.0094(5) | 0.0074(5) |

**TABLE 5.**–*continued*

| | BHT50_2 | BHT070_1 | BHT120_6 | BHT095_2 | BHT100_2 | BHT110n1 | BHT120n2 | BHT130_2 | BHT140_2 |
|---|---|---|---|---|---|---|---|---|---|
| Crystal data | | | | | | | | | |
| $x$ $Al^{3+}_{tot}$ | 0.590 | 0.663 | 0.789 | 0.866 | 0.909 | 0.986 | 1.078 | 1.259 | 1.356 |
| Space group | *I2mb* | *I2mb* | *I2mb* | *I2mb* | *I2mb* | *I2mb* | *I2mb* | *I2mb* | *I2mb* |
| $a$ (Å) | 5.3832(2) | 5.3714(3) | 5.3569(2) | 5.3510(2) | 5.3469(3) | 5.3369(2) | 5.3269(3) | 5.3093(3) | 5.2991(4) |
| $b$ (Å) | 14.6214(7) | 14.5805(7) | 14.5407(7) | 14.5256(8) | 14.5149(8) | 14.4945(7) | 14.4687(9) | 14.4534(8) | 14.4434(9) |
| $c$ (Å) | 5.5916(3) | 5.5847(3) | 5.5735(3) | 5.5685(3) | 5.5640(3) | 5.5548(3) | 5.5433(2) | 5.5230(3) | 5.5099(3) |
| $V$ (Å$^3$) | 440.11 | 437.38 | 434.14 | 432.82 | 431.82 | 429.70 | 427.24 | 423.82 | 421.71 |
| $M_r$ | 254.83 | 252.72 | 249.98 | 246.87 | 245.62 | 243.39 | 240.74 | 235.51 | 232.71 |
| $D_{calc}$ (g/cm$^3$) | 3.846 | 3.838 | 3.811 | 3.788 | 3.778 | 3.762 | 3.743 | 3.691 | 3.665 |
| μ (mm$^{-1}$) | 7.088 | 6.914 | 6.587 | 6.376 | 6.260 | 6.057 | 5.811 | 5.301 | 5.028 |
| shape | platy | platy | cuboid | platy | platy | prismatic | cuboid | cuboid | prismatic |
| size max. (mm) | 0.27 | 0.19 | 0.14 | 0.15 | 0.18 | 0.20 | 0.19 | 0.19 | 0.20 |
| Data collection | | | | | | | | | |
| 2θmax (°) | 56.12 | 56.07 | 56.37 | 55.89 | 56.08 | 56.33 | 56.33 | 56.38 | 56.28 |
| $h$ $k$ $l$ range: $h$ | −7 → 7 | −7 → 7 | −6 → 7 | −6 → 6 | −6 → 7 | −7 → 7 | −6 → 7 | −6 → 6 | −7 → 6 |
| $k$ | −19 → 18 | −19 → 19 | −19 → 18 | −18 → 18 | −18 → 18 | −17 → 18 | −18 → 18 | −18 → 18 | −18 → 18 |
| $l$ | −7 → 7 | −7 → 7 | −7 → 7 | −7 → 7 | −7 → 7 | −7 → 7 | −7 → 7 | −7 → 7 | −6 → 7 |
| $T_{min.}$ | 0.339 | 0.365 | 0.397 | 0.375 | 0.281 | 0.346 | 0.309 | 0.369 | 0.573 |
| $T_{max.}$ | 0.459 | 0.504 | 0.508 | 0.677 | 0.651 | 0.531 | 0.398 | 0.424 | 0.654 |
| $N_{measured}$ | 2134 | 2020 | 1887 | 2008 | 1968 | 2029 | 1992 | 2027 | 2032 |
| $N_{independent}$ | 533 | 506 | 533 | 521 | 526 | 498 | 506 | 529 | 512 |
| $R_{int}$ (%) | 3.99 | 3.97 | 2.62 | 3.35 | 4.04 | 4.49 | 7.13 | 3.12 | 3.72 |
| $\|E^2 - 1\|$ | 0.764 | 0.772 | 0.776 | 0.792 | 0.793 | 0.793 | 0.793 | 0.798 | 0.811 |
| Refinement | | | | | | | | | |
| $N_{parameters}$ | 50 | 50 | 50 | 49 | 49 | 49 | 49 | 49 | 49 |
| $R_1 > 4s$ (%) | 1.70 | 1.90 | 1.40 | 2.13 | 1.83 | 1.99 | 2.38 | 1.93 | 2.17 |
| $R_1$ all (%) | 1.83 | 2.12 | 1.49 | 2.27 | 1.99 | 2.37 | 2.68 | 2.35 | 2.44 |
| $wR_2 > 4s$ (%) | 4.04 | 4.28 | 3.32 | 5.44 | 4.39 | 4.06 | 5.34 | 4.17 | 5.25 |
| $wR_2$ all (%) | 4.21 | 4.66 | 3.32 | 5.89 | 4.69 | 4.51 | 5.93 | 4.41 | 5.63 |
| G.O.F | 1.120 | 1.162 | 1.100 | 1.168 | 1.168 | 1.146 | 1.118 | 0.971 | 1.136 |
| $\Delta\rho_{min}$ (e/Å$^3$) | −0.31 | −0.48 | −0.25 | −0.49 | −0.37 | −0.46 | −0.68 | −0.45 | −0.43 |
| $\Delta\rho_{max}$ (e/Å$^3$) | 0.33 | 0.45 | 0.29 | 0.57 | 0.41 | 0.52 | 0.64 | 0.45 | 0.47 |
| weights $w$ ($a$, $b$) | 0.0262 | 0.0253 | 0.0207 | 0.0427 | 0.0283 | 0.0218 | 0.0295 | 0.0237 | 0.0351 |
| Extinction $k$ | 0.0056 | 0.0029 | 0.0040 | none | none | none | none | none | none |

**TABLE 6.**–*continued*

| | | BHT50_2 | BHT070_1 | BHT120_6 | BHT095_2 | BHT100_2 | BHT110n1 | BHT120n2 | BHT130_2 | BHT140_2 |
|---|---|---|---|---|---|---|---|---|---|---|
| Ca | $x$ | 0.4912(1) | 0.4911(1) | 0.49115(9) | 0.4913(1) | 0.49141(9) | 0.4914(1) | 0.4914(1) | 0.4917(2) | 0.4919(1) |
| | $y$ | 0.10820(3) | 0.1083(1) | 0.10854(2) | 0.10859(3) | 0.10855(3) | 0.10852(3) | 0.10871(4) | 0.10850(3) | 0.10859(3) |
| | $z$ | 0.02655(7) | 0.0265(1) | 0.02705(6) | 0.02718(8) | 0.02702(8) | 0.02709(9) | 0.0271(1) | 0.02695(9) | 0.0266(1) |
| | $U_{eq}$ | 0.0063(2) | 0.0066(2) | 0.0076(1) | 0.0062(2) | 0.0069(2) | 0.0064(2) | 0.0073(2) | 0.0074(2) | 0.0091(2) |
| M-site | $x$ | 0.0011(1) | 0.0006(1) | 0.0006(1) | 0.0005(2) | 0.0006(1) | 0.0004(1) | 0.0004(2) | −0.0003(2) | −0.0004(2) |
| | $y$ | 0 | 0 | 0 | 0 | 0 | 0 | 0 | 0 | 0 |
| | $z$ | 0 | 0 | 0 | 0 | 0 | 0 | 0 | 0 | 0 |
| | $U_{eq}$ | 0.0030(3) | 0.0032(2) | 0.0047(2) | 0.0037(2) | 0.0044(2) | 0.0036(2) | 0.0044(3) | 0.0049(2) | 0.0071(3) |
| | Occ. Fe | 0.849(5) | 0.851(5) | 0.791(4) | 0.783(5) | 0.758(6) | 0.733(4) | 0.684(5) | 0.594(4) | 0.541(4) |
| | Occ. Al | 0.151(5) | 0.149(5) | 0.209(4) | 0.217(5) | 0.242(6) | 0.267(4) | 0.316(5) | 0.406(4) | 0.459(4) |
| T-site | $x$ | 0.9523(1) | 0.9528(2) | 0.9528(1) | 0.9527(2) | 0.9524(2) | 0.9526(2) | 0.9526(2) | 0.9527(2) | 0.9527(2) |
| | $y$ | 1/4 | 1/4 | 1/4 | 1/4 | 1/4 | 1/4 | 1/4 | 1/4 | 1/4 |
| | $z$ | 0.9300(1) | 0.9296(2) | 0.92900(9) | 0.9283(1) | 0.9283(1) | 0.9278(2) | 0.9275(2) | 0.9270(2) | 0.9264(2) |
| | $U_{eq}$ | 0.0023(2) | 0.0016(2) | 0.0043(2) | 0.0027(3) | 0.0036(2) | 0.0025(3) | 0.0030(4) | 0.0031(2) | 0.0054(4) |
| | Occ. Fe | 0.561(5) | 0.486(5) | 0.420(4) | 0.351(4) | 0.333(6) | 0.281(4) | 0.238(5) | 0.147(4) | 0.113(5) |
| | Occ. Al | 0.439(5) | 0.514(5) | 0.580(4) | 0.649(4) | 0.667(6) | 0.719(4) | 0.762(5) | 0.853(4) | 0.887(5) |
| O1 | $x$ | 0.2494(4) | 0.2501(5) | 0.2494(3) | 0.2494(5) | 0.2484(4) | 0.2486(5) | 0.2481(5) | 0.2485(5) | 0.2481(5) |
| | $y$ | 0.98593(9) | 0.9860(1) | 0.98611(7) | 0.9864(1) | 0.9865(1) | 0.9864(1) | 0.9868(1) | 0.9871(1) | 0.9875(1) |
| | $z$ | 0.2531(4) | 0.2530(6) | 0.2530(4) | 0.2529(4) | 0.2528(4) | 0.2519(6) | 0.2535(7) | 0.2536(7) | 0.2522(5) |
| | $U_{eq}$ | 0.0060(3) | 0.0064(4) | 0.0074(3) | 0.0062(4) | 0.0068(3) | 0.0061(4) | 0.0072(5) | 0.0073(4) | 0.0090(4) |
| O2 | $x$ | 0.0238(4) | 0.0240(4) | 0.0228(3) | 0.0216(4) | 0.0215(4) | 0.0203(4) | 0.0200(5) | 0.0196(5) | 0.0185(4) |
| | $y$ | 0.1426(1) | 0.1429(2) | 0.14334(9) | 0.1433(1) | 0.1435(1) | 0.1440(1) | 0.1437(2) | 0.1438(1) | 0.1438(1) |
| | $z$ | 0.0697(3) | 0.0697(4) | 0.0691(2) | 0.0686(3) | 0.0686(3) | 0.0674(4) | 0.0666(4) | 0.0662(4) | 0.0648(4) |
| | $U_{eq}$ | 0.0085(4) | 0.0097(5) | 0.0101(3) | 0.0088(5) | 0.0093(4) | 0.0095(5) | 0.0101(5) | 0.0110(5) | 0.0118(5) |
| O3 | $x$ | 0.6102(5) | 0.6106(5) | 0.6135(4) | 0.6146(6) | 0.6151(4) | 0.6172(5) | 0.6168(7) | 0.6184(6) | 0.6183(6) |
| | $y$ | 1/4 | 1/4 | 1/4 | 1/4 | 1/4 | 1/4 | 1/4 | 1/4 | 1/4 |
| | $z$ | 0.8677(4) | 0.8552(6) | 0.8640(4) | 0.8633(5) | 0.8620(5) | 0.8608(5) | 0.8610(6) | 0.8586(5) | 0.8593(6) |
| | $U_{eq}$ | 0.0072(5) | 0.0084(7) | 0.0083(4) | 0.0070(6) | 0.0077(5) | 0.0063(6) | 0.0082(7) | 0.0070(6) | 0.0093(6) |

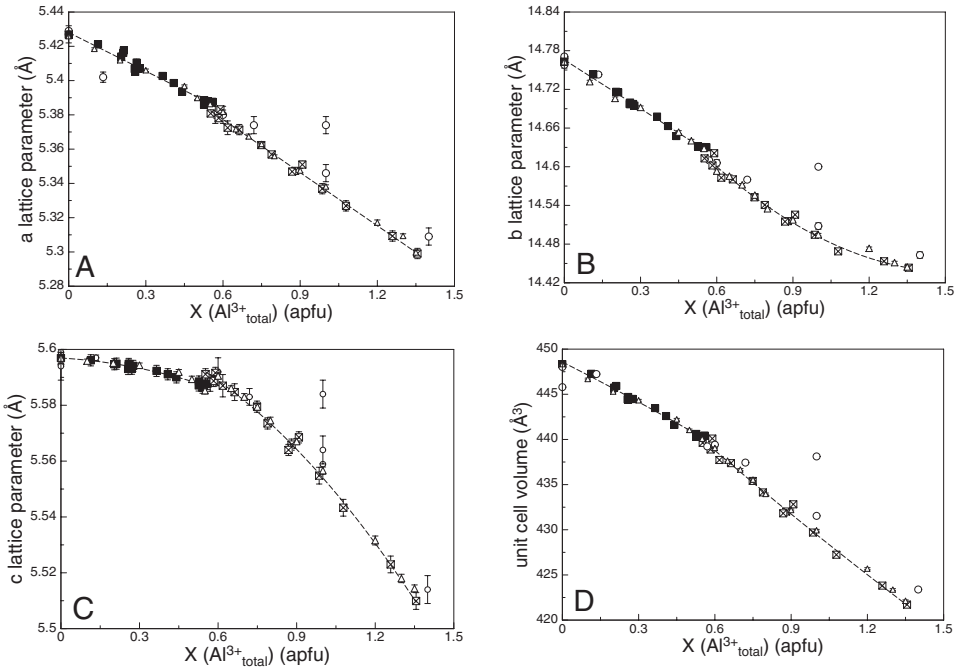


**FIGURE 8.** Compositional variations of unit-cell parameters for the $Ca_2Fe_{2-x}Al_xO_5$ solid solution series at 25 °C. In this and the following figure filled and open symbols correspond to samples with *Pnma* and *I2mb* symmetry, respectively. Open triangles represent data for samples synthesized by ceramic sintering at 1300 °C; the open circles represent data from the literature (Woermann et al. 1968; Colville and Geller 1971, 1972; Colville 1970; Kahlenberg and Fischer 2000; linear or quadratic regression curves are fitted to the data and serve as guides to the eye; if not visible, estimated standard deviations are smaller than the symbols, and the filled and open symbols correspond to *Pnma* and *I2mb* symmetry of the samples.

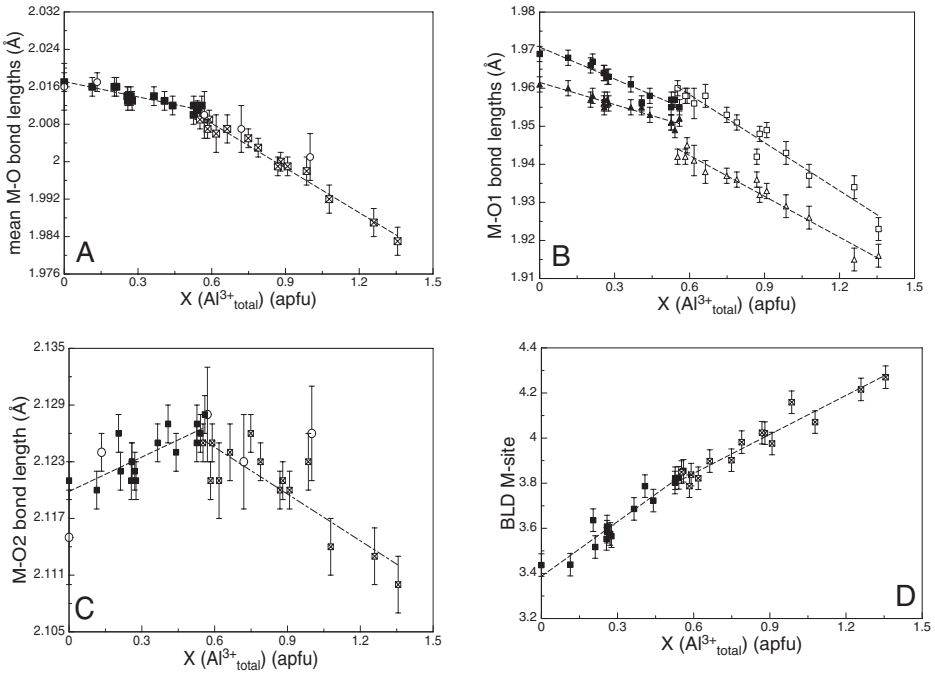


**FIGURE 9.** Average (**a**) and individual M-O bond lengths (**b-c**) and bond length distortion (BLD) values for the $Ca_2Fe_{2-x}Al_xO_5$ solid-solution series at 25 °C. Open circles in (**a**) are data from the literature (Woermann et al. 1968; Colville and Geller 1971, 1972; Colville 1970; Kahlenberg and Fischer 2000); regression lines are fitted to the data and serve as guides to the eye; if not visible, estimated standard deviations are smaller than the symbols, and the filled and open symbols correspond to *Pnma* and *I2mb* symmetry of the samples.

interconnecting the octahedra by corner sharing, decrease by 0.5 and 0.7% from $x = 0.0$ to $x = 0.56$ (*Pnma* phase), whereas the M-O2 bond lengths (Fig. 9c) increase slightly by ≈0.3%. At the phase transition a significant jump in M-O1 bond lengths is observed and the course of M-O2 vs. $Al^{3+}_{tot}$ data changes the slope direction. For $x > 0.56$, all three non-equivalent M-O bond lengths decrease with increasing $Al^{3+}_{tot}$ content, the M-O1 bonds by 1.5 and 1.7%, the M-O2 bond by 0.7%. Because of the non-uniform decrease of M-O bond lengths, the bond length distortion (BLD, Renner and Lehmann 1986) of the octahedral site increases with increasing $Al^{3+}_{tot}$ content (Fig. 9d).

The *Pnma-I2mb* phase transition is also reflected in the average of the O-O distances, defining the edges of the $(Fe^{3+},Al^{3+})O_6$ octahedron (deposit Fig. 10a[3]). As the point symmetry of the octahedron changes from $\bar{1}$ (*Pnma*) to 2 (*I2mb*), the number of non-equivalent O1-O1 distances within the equatorial plane of the octahedron changes from 2 in *Pnma* to 3 in *I2mb*. The M cation, located at (0, 0, 0) in *Pnma*, is slightly displaced along *a* in *I2mb* (*x*, 0, 0) thus allowing the two equivalent O1-O1 distances [2.840(2) Å] in $Ca_2Fe_2O_5$ to become inequivalent. Together with the displacements of the O1 atom, this leads to a rather large change in lengths for these O1-O1 octahedral edges at the phase transition (deposit Fig. 10b[3]). The O1-O2 interatomic distances defining the edges between equatorial O atoms and the apex O atoms of the octahedra display only small composition-dependent changes (decrease and increase) for the *Pnma* phase (Fig. 10c), consistent with the small increase observed for the M-O2 bond length (deposit Fig. 10a[3]). Linear decreases with increasing $Al^{3+}_{tot}$ content, however with different slopes, take place for the O1-O2 edge lengths in the body-centered phase (deposit Fig. 10c[3]). The edge length distortion (ELD) parameter (deposit Fig. 10d[3]) as defined by Renner and Lehmann (1986) increases from $Ca_2Fe_2O_5$ to samples with $x \approx 0.56$. The phase transition is associated with a sudden increase of ELD, which then slightly decreases with increasing $Al^{3+}_{tot}$ content for the body-centered phase.

Octahedral bond angles O-M-O range between 86.6(1)° and 93.4(1)° in $Ca_2Fe_2O_5$. The incorporation of $Al^{3+}$ slightly modifies the O-M-O bond angles. The changes are moderate and less than ≈1° over the complete solid solution series. At the phase transition, discontinuities are present for all non-equivalent bond angles; the situation is shown for the O1-M-O2 bond angle as an example (deposit Fig. 11a[3]). The quadratic octahedral angle variance OAV, as defined by Robinson et al. (1971), exhibits this discontinuity in a pronounced way (deposit Fig. 11b[3]). In terms of the OAV, samples with $x \approx 0.6$ have the greatest deviation from ideal octahedral geometry. Increasing the $Al^{3+}_{tot}$ content decreases the bond-angle distortion. As depicted in deposit Figure 11b[3] the O1-M-O2 bond angles approach the ideal value of 90° with increasing $Al^{3+}$ substitution. This is also observable for the other O-M-O bond angles (cf. deposit Table 8[2]) and reflects the substitution of the 3*d* cation $Fe^{3+}$ by the closed shell cation $Al^{3+}$, having different covalence character (directed to non-directed bonds).

As outlined in Figure 1, octahedra are tilted against each other by rotation about [1 0 0] and [0 1 0]. In $Ca_2Fe_2O_5$ the octahedra are rotated by 9.8° around [1 0 0] and by 3.1° around [1 0]. With increasing $Al^{3+}_{tot}$ content, the tilt around [0 1 0] (Fig. 12a) decreases by ≈1° within the *Pnma* phase. Similar to perovskite, the tilt is due to the fact that the octahedra are too large for the cation (here $Ca^{2+}$) within the interstitial site. Reducing the overall size of the octahedra (by substituting the smaller $Al^{3+}$ cation for $Fe^{3+}$) also reduces the octahedral tilt. The phase transition is associated with a sudden decrease of the octahedral tilting by ≈0.5°. In samples with *I2mb* symmetry, the tilting around b continues to decrease with increasing $Al^{3+}_{tot}$ down to ≈7.5°. For samples with *Pnma* symmetry the tilting around [1 0 0] also decreases with increasing $Al^{3+}_{tot}$ content. The discontinuity at the phase transition is even more pronounced (Fig. 12b). In contrast to the tilt around [0 1 0], no significant reduction of tilt around [1 0 0] is observed for the *I2mb* phase.

**Tetrahedral site.** In $Ca_2Fe_2O_5$ the tetrahedral bonds show lengths of 1.843(2) Å for the T-O2 and 1.912(2)-1.914(2) Å for the T-O3 bonds. The shorter T-O2 bonds are those connecting the tetrahedral chain with the octahedral layer, while the T-O3 bonds are those within the tetrahedral chain running along [1 0 0]. With increasing $Al^{3+}$ substitution, T-O bonds decrease distinctly following a linear trend (deposit Figs. 13a and 13b[3]) for the *Pnma*

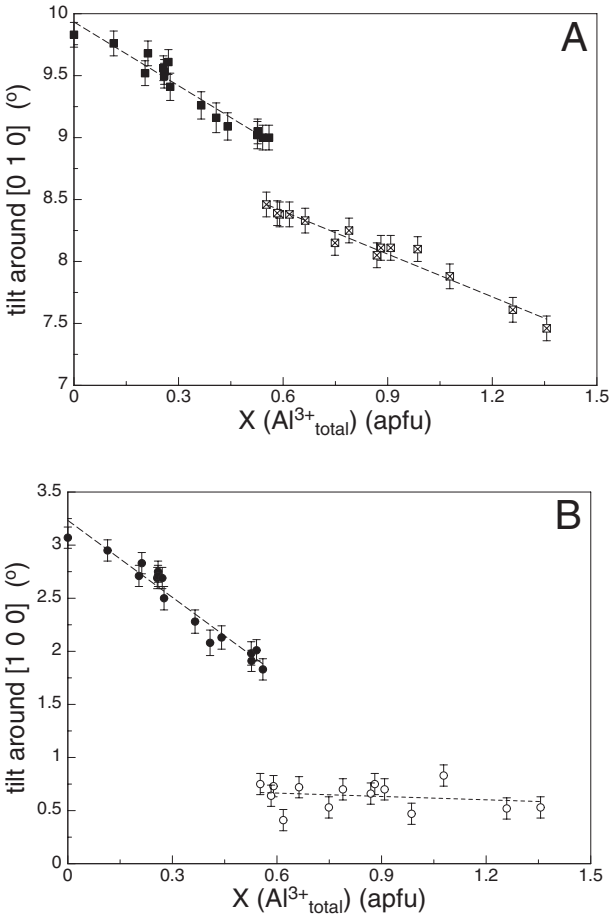


**FIGURE 12.** Tilting of the octahedra around [1 0 0] (**a**) and [0 1 0] (**b**) for samples of the $Ca_2Fe_{2-x}Al_xO_5$ solid solution series at 25 °C. Regression lines are fitted to the data and serve as guides to the eye; and the filled and open symbols correspond to *Pnma* and *I2mb* symmetry of the samples.

phase. At the phase transition a small jump toward lower values can be seen for the T-O3 bonds. For the *I2mb* phase, the variation of T-O bonds exhibit a different slope compared to the samples of the *Pnma* phase. A non-linear course of the T-O2 vs. $Al^{3+}_{tot}$ (deposit Fig. 13b[3]) and of the <T-O> vs. $Al^{3+}_{tot}$ data is observable at high $Al^{3+}$ contents (deposit Fig. 13c[3]).

The O-O interatomic distances in $Ca_2Fe_2O_5$, defining the edges of the tetrahedron, can also be divided into two groups. Three out of the four are within 3.008(1) and 3.048(2) Å (Fig. 14a), but the fourth distance (O2-O2) is distinctly longer at 3.229(2) Å (Fig. 14b). This is the tetrahedral edge, connecting the two octahedral layers along [0 1 0]. As for the T-O bonds, tetrahedral edges vary linearly with increasing $Al^{3+}_{tot}$ content in the *Pnma* phase and exhibit some compositionally dependent non-linear behavior at high $Al^{3+}$ concentrations.

The average O-T-O angle is close to the ideal value of 109.4° with no significant compositionally dependent variation. The individual bond angles, however, range between 105.4(1)° and 122.2(1)° in $Ca_2Fe_2O_5$. The largest value occurs for the angle between the tetrahedral cation T and the two O2 atoms shared by the tetrahedral chain and two neighboring octahedral sheets. This corresponds to an elongation of the tetrahedron along *b*. The large O2-T-O2 angle is consistent with the large O2-O2 edge length (Fig. 14a). Substituting $Fe^{3+}$ by $Al^{3+}$ causes a non uniform variation of the O2-T-O2 angle. For the *Pnma* phase (Fig. 15a) it decreases linearly with increasing $Al^{3+}_{tot}$ content. In the *I2mb* phase this trend continues up to $x \approx 0.75$. Beyond this $Al^{3+}_{tot}$ content the slope changes sign and the O2-T-O2 angle increases with increasing $Al^{3+}_{tot}$ content. This behavior is related to the reduced decrease of the O2-O2 tetrahedral edge. As the T-O2 bond continuously decreases, but the change of the O2-O2 bond becomes non-linearly reduced at high $Al^{3+}_{tot}$ contents, the course of the O2-T-O2 bond angle vs. $Al^{3+}_{tot}$ data have to show a positive slope at high $Al^{3+}_{tot}$ contents. The O3-T-O3 angle (Fig. 15b) increases, first slightly non-linearly in *Pnma*, and, after a small discontinuity at the phase transition, linearly in *I2mb*. This increase in O3-T-O3 indicates that increasing $Al^{3+}$ stretches the distorted tetrahedron slightly in the chain direction, which is parallel to the *a* axis. One of the two O2-T-O3 angles (Fig. 15b) decreases with increasing $Al^{3+}$, the others increase at the same extent within the *Pnma* phase. For the *I2mb* phase both angles decrease. The large spread in tetrahedral bond angles is also observed in large values of the quadratic tetrahedral angle variance TAV (Fig. 15c) as defined by Robinson et al. (1971). For pure $Ca_2Fe_2O_5$ this amounts to 39.6°. The approach of O-T-O angles to more ideal values (decrease of O2-T-O2, increase of O3-T-O3 and one O2-T-O3 angle) lowers the TAV within the *Pnma* phase. It is mainly the inflection of O2-T-O2 vs. $Al^{3+}_{tot}$ data which causes the TAV to increase again at high $Al^{3+}_{tot}$ contents within the *I2mb* phase. The tetrahedral chains are strongly kinked, expressed by low O3-O3-O3 angles (Fig. 15d). Increasing $Al^{3+}$ causes an increase of this angle, i.e., the tetrahedral chains become more stretched. This stretching is in close relationship with the decreasing tilting of the octahedra.

**Interstitial site ($Ca^{2+}$).** The $Fe^{3+}$ by $Al^{3+}$ substitution primarily affects the octahedral and the tetrahedral site, however it is also reflected in the geometry of the Ca site. The calcium ion is surrounded by a irregular polyhedron of eight O atoms at distances ranging from 2.323(2) to 3.000(2) Å. Figure 16 gives a comparison of the next neighbor geometry of the $Ca^{2+}$ cation in *Pnma* ($x = 0.00$) and *I2mb* ($x = 1.34$) symmetry respectively. The mean of the eight different Ca-O bond lengths decreases linearly with $Al^{3+}$ for both the *Pnma* and the *I2mb* phase, however with different slopes and a slight jump at the phase transition (Fig. 17a). The individual Ca-O bond lengths show different compositional variation in *Pnma* and *I2mb*. The change in octahedral tilting distinctly alters the O1 environment around the Ca atom and thus is closely related to the changes in individual Ca-O1 bond lengths. The rapid reduction of the octahedral tilt at the phase transition causes rapid changes in Ca-O1 bond lengths (Fig. 17b-c), most evident for the long Ca-O1 bond at 2.732(2) Å in $Ca_2Fe_2O_5$ (Fig. 17c). A smaller and nearly continuous reduction by 0.7% for the complete compositional range is observed for the Ca-O2 bond at 2.323(2) Å in $Ca_2Fe_2O_5$. The Ca-O2 bonds connect the $Ca^{2+}$ cation to both the tetrahedral chain and the octahedral sheet. The Ca-O2 bond at 2.542(2) Å in $Ca_2Fe_2O_5$

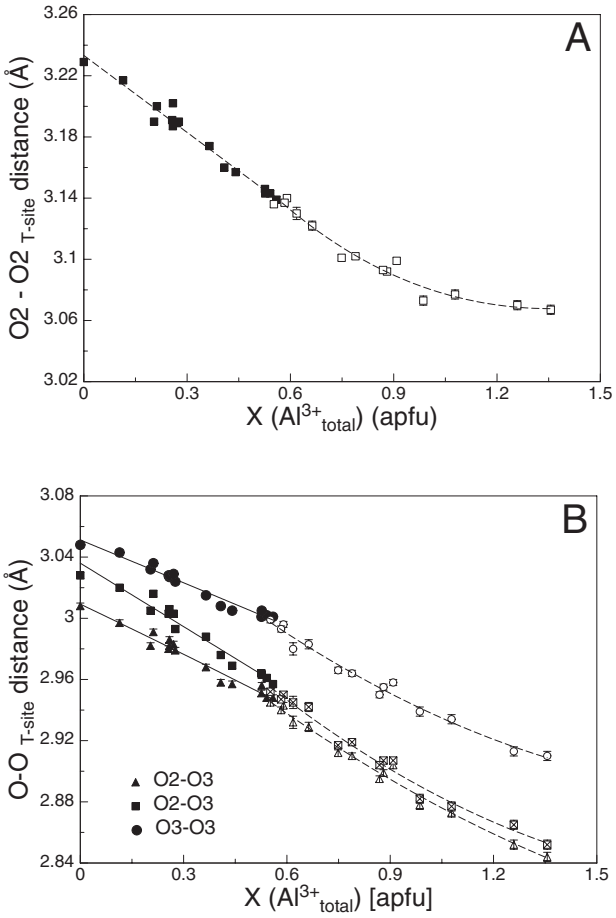


**FIGURE 14.** O-O atom distances defining the edges of the tetrahedron for samples of the $Ca_2Fe_{2-x}Al_xO_5$ solid solution series at 25 °C. Regression curves are fitted to the data and serve as guides to the eye; if not visible, estimated standard deviations are smaller than the symbols, and the filled and open symbols correspond to *Pnma* and *I2mb* symmetry of the samples.

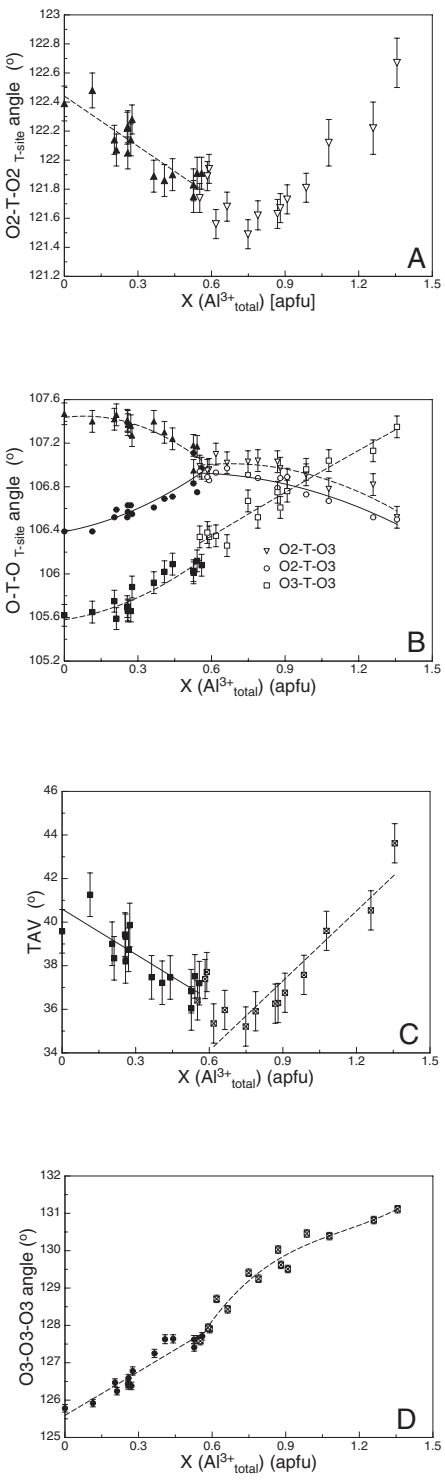


**FIGURE 15.** Individual O-T-O bond angles of the tetrahedral site for samples of the $Ca_2Fe_{2-x}Al_xO_5$ solid-solution series at 25 °C. Regression curves are fitted to the data and serve as guides to the eye; if not visible, estimated standard deviations are smaller than the symbols, and the filled and open symbols correspond to *Pnma* and *I2mb* symmetry of the samples.

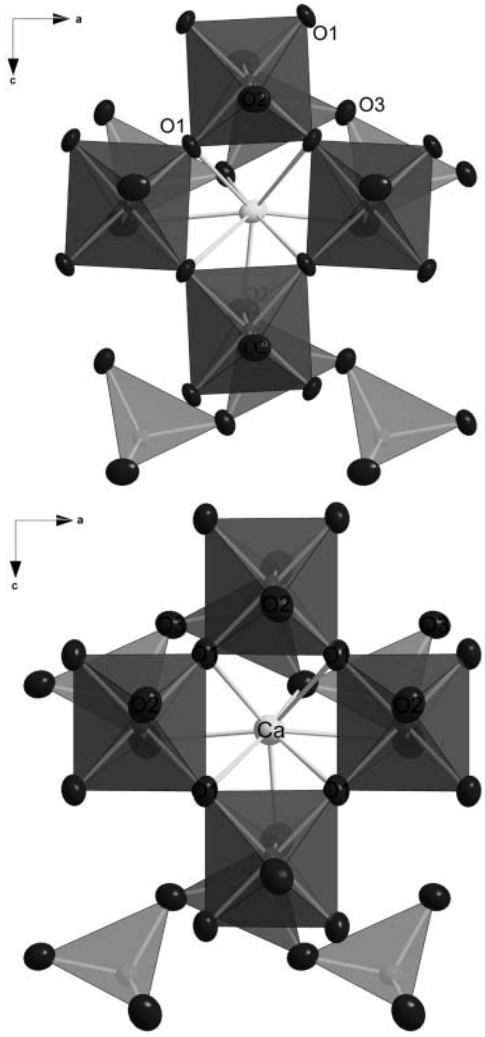


**FIGURE 16.** Comparison of the geometry around the $Ca^{2+}$ cation in a projection along b for $Ca_2Fe_2O_5$ with *Pnma* symmetry (**a**) and for $Ca_2Fe_{0.64}Al_{1.36}O_5$ with *I2mb* symmetry. Note that in *I2mb* the octahedra have a nearly rectangular arrangement.

increases by 0.9% within the *Pnma* phase, while the Ca-O2 bond at 3.000(2) Å in $Ca_2Fe_2O_5$ decreases by 2.4% within the same compositional range. For the *I2mb* phase all Ca-O2 bonds decrease with increasing $Al^{3+}$. These changes are related to changes in the buckling (kinking) of the tetrahedral chain. The Ca-O3 bond (Fig. 17d), connecting the $Ca^{2+}$ cation to the bridging O3 atom of the tetrahedral chain, remains rather constant over the whole compositional range. The jump in octahedral tilting and within the Ca-O1 bond lengths at the phase transition is related to the discontinuous movement of the Ca($x$) and O1($x$) and O1($z$) fractional atomic co-ordinates. The above mentioned co-ordinates as well as Ca($z$) change steadily increases with increasing $Al^{3+}$ up to the phase transition, at higher $Al^{3+}$ contents their numeric values stay nearly constant, correlating with an almost constant tilt angle around [1 0 0]. The reduction of the tilt with increasing Al-content is directly related to a stretching of the tetrahedral chains along the $a$ - axis. Tetrahedral chain and octahedral layer are connected to each other by the O2 oxygen

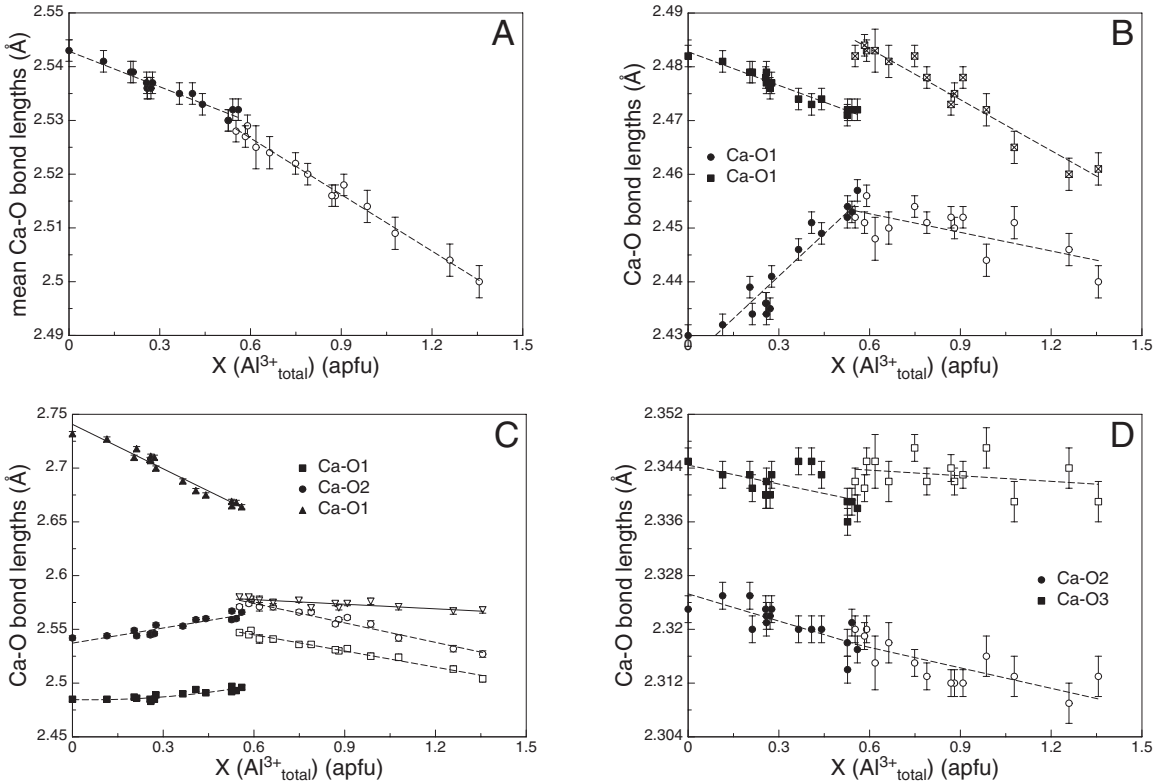


**FIGURE 17.** Average (**a**) and individual (**b–d**) Ca-O bond lengths for samples of the $Ca_2Fe_{2-x}Al_xO_5$ solid-solution series at 25 °C. Regression curves are fitted to the data and serve as guides to the eye; if not visible, estimated standard deviations are smaller than the symbols, and the filled and open symbols correspond to *Pnma* and *I2mb* symmetry of the samples.

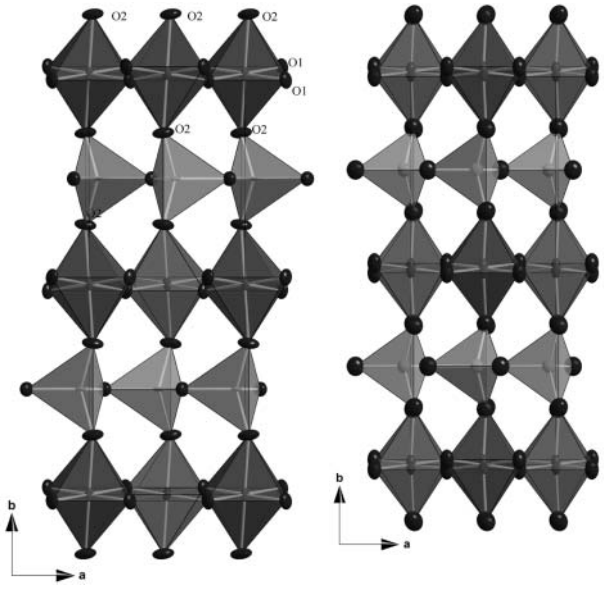


**FIGURE 18.** Comparison of the structural topology in a projection along c for $Ca_2Fe_2O_5$ with *Pnma* symmetry (**a**) and $Ca_2Fe_{0.64}Al_{1.36}O_5$ (**b**) with *I2mb* symmetry displaying the different stacking sequences of the tetrahedral chains.

atom. The kinking of tetrahedral chains decreases by ≈5.5° from $Ca_2Fe_2O5$ to $Ca_2Fe_{0.64}Al_{1.34}O_5$, but the chains remain buckled also in *I2mb*. Similar to perovskite, the underlying reason for the tilt of the octahedra can be found in the size of the $Ca^{2+}$ cation in the interstitial site of the structure. The movement of the O1 oxygen atom in *x*, *y* and *z* directions gives rise to a symmetric nearly rectangular arrangement of octahedra within the *a–c* plane in *I2mb*, while, in *Pnma* (Fig. 16), the arrangement is much more distorted. Projected onto the *a-c* plane, the O1-O1-O1 angle is 179.0(1)° along the *a* axis and exactly 180° along the *c* - axis in *I2mb*. One further distinct difference between the *Pnma* and the *I2mb* structure concerns the tetrahedral chain. Whereas the chain of tetrahedra at x/a = ¼ are essentially the same in both structures (Fig. 18), the chains at x/a = ¾ are related to each other by an inversion center (–1) in *Pnma* and by a twofold axis is *I2mb*. Thus the tetrahedra have a different orientation along the *b* - axis and build up a stacking sequence of O-T-O-T‘-... for *Pnma*, whereas it is O-T-O-T-... for *I2mb*.

**Cation distribution.** By refining the site occupation number for the octahedral and tetrahedral site it was possible to determine the cation distribution of $Fe^{3+}$ and $Al^{3+}$ over the corresponding sites. Our results show that the distribution is far from random and that $Al^{3+}$ strongly prefers the tetrahedral site (Fig. 19). However, even at low $Al^{3+}$ contents, $Al^{3+}$ enters the octahedral and the tetrahedral site for both types of samples, those grown directly from the melt and quenched from 1300 °C (BHT samples) as well as for samples grown with flux methods and quenched from

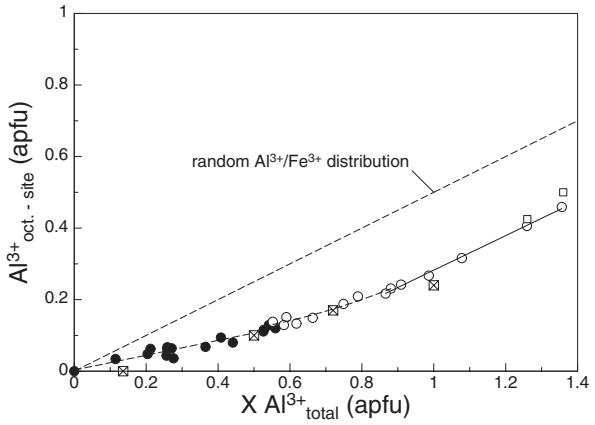


**FIGURE 19.** Content of $Al^{3+}$ at the octahedral site, indicating a distinct preference of $Al^{3+}$ for the tetrahedral site for samples of the $Ca_2Fe_{2-x}Al_xO_5$ solid solution series at 25 °C. Regression curves are fitted to the data and serve as guides to the eye, filled and open symbols correspond to *Pnma* and *I2mb* symmetry of the samples, and open crossed squares are data from the literature.

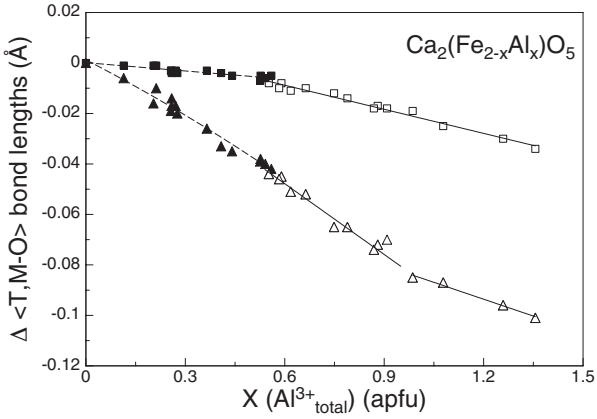


**FIGURE 20.** Changes in average octahedral and tetrahedral bond lengths relative to the values of $Ca_2Fe_2O_5$ for samples of the $Ca_2Fe_{2-x}Al_xO_5$ solid solution series at 25 °C. Filled and open circles represent data from this study, the open squares represent data obtained from Mössbauer spectroscopy, and the open crossed squares represent data from the literature (Colville 1970; Colville and Geller 1971, 1972). Regression curves are fitted to the data and serve as guides to the eye; if not visible, estimated standard deviations are smaller than the symbols, and the filled and open symbols correspond to *Pnma* and *I2mb* symmetry of the samples.

900 °C. Mössbauer spectroscopy has been used to check the cation distribution found in the present study by site occupation refinement from single crystal intensity data. The results of the two different methods are in good agreement: sample BHT140 ($x = 1.36$) was found to contain 0.103(5) and 0.144(7) $Fe^{3+}$ atoms per formula unit at the tetrahedral site, as determined by site-occupation refinement of single crystal X-ray intensity data and by Mössbauer spectroscopy, respectively. Similar agreement was found for sample BHT130 ($x = 1.26$) with 0.147(4) and 0.166(8) $Fe^{3+}$ apfu and sample BHT120 ($x = 1.078$) with 0.238(5) and 0.235(11) $Fe^{3+}$ apfu. The cation distribution obtained for our samples is in good agreement with that of Colville and Geller (1971, 1972). Their data are indicated by open crossed squares in Figure 19. Smith (1962) proposed that $Al^{3+}$ preferentially enters the tetrahedral site until half the tetrahedra are filled, after which additional $Al^{3+}$ and $Fe^{3+}$ atoms distribute equally. Figure 19 shows that this view is supported by our data. Above $x \approx 0.9$, corresponding to ≈0.65 $Al^{3+}$ apfu at the tetrahedral site, the trend of the data points for $Al^{3+}_{tot}$ vs. $Al^{3+}_{oct}$ follows a straight line with a slope that is almost identical to that for an equal distribution of $Al^{3+}$ and $Fe^{3+}$ over octahedral and tetrahedral sites respectively. These findings show that above an $\approx 2/3$ filling of the tetrahedral site by $Al^{3+}$ additional $Al^{3+}$, which substitutes for $Fe^{3+}$, distributes equally over the octahedral and the tetrahedral site. The non-linear variation of especially T-O2 and <T-O> at high $Al^{3+}$ contents can be ascribed to the change in $Al^{3+}$ site preference, i.e., the equal distribution of additional $Al^{3+}$ over M and T sites. A reason for the change of symmetry from *Pnma* to *I2mb* may also be found in the preference of $Al^{3+}$ for the tetrahedral site at low overall $Al^{3+}$ contents. As the tetrahedral chains incorporate more $Al^{3+}$ than the octahedral layer, the tetrahedra shrink and chains can straighten to produce the higher *I2mb* symmetry. A second source of information on the Fe/Al-distribution can be found in the average bond lengths. The relative change of average octahedral and tetrahedral bond lengths within the Fe/Al binary join is markedly different at low overall $Al^{3+}$ contents (Fig. 20). Above $x \approx 0.9$ the two graphs (changes of average T-O and average M-O bond lengths relative to $Ca_2Fe_2O_5$) are almost parallel, supporting the above proposal.

## ACKNOWLEDGMENTS

G.J.R. wishes to thank the Austrian Academy of Science for financial support throughout an APART (Austrian Program for Advanced Research and Technology) scholarship during 2000–2003. The technical support of J. Ernst (Aachen) for the synthesis and of V. Kaiser (Aachen) in the X-ray laboratory is gratefully acknowledged. The careful and thorough review and the helpful comments of G. Cruciani and an anonymous referee as well as those of S. Quartieri are gratefully acknowledged.

## REFERENCES CITED

Aggarwal, P.S., Gard, J.A., and Glasser, F.P. (1972) Synthesis and properties of dicalcium aluminate, $2CaO \cdot Al_2O_3$. Cement and Concrete Research, 2, 291–297.

Aldebert, P. and Traverse, J.P. (1984) $\alpha$-$Al_2O_3$: A high-temperature thermal expansion standard. High Temperature-High Pressure, 16, 127–135.

Berastegui, P., Eriksson, S.-G., and Hull, S. (1999) A neutron diffraction study of the temperature dependence of $Ca_2Fe_2O_5$. Materials Research Bulletin, 34, 303–314.

Bertaut, E.F., Blum, P., and Sagnières, A. (1959) Structure du ferrite bicalcique et de la brownmillerite. Acta Crystallographica, 12, 149–159.

Colville, A.A. (1970) The crystal structure $Ca_2Fe_2O_5$ and its relation to the nuclear electric field gradient at the iron sites. Acta Crystallographica, B26, 1469–1473.

Colville, A.A. and Geller, S. (1971) The crystal structure of brownmillerite, $Ca_2FeAlO_5$. Acta Crystallographica, B27, 2311–2315.

——— (1972) Crystal structures of $Ca_2Fe_{1.43}Al_{0.57}O_5$ and $Ca_2Fe_{1.28}Al_{0.72}O_5$. Acta Crystallographica, B28, 3196–3200.

Fukuda, K. and Ando, H. (2002) Determination of the *Pcmn*/*Ibm*2 phase boundary at high temperatures in the system $Ca_2Fe_2O_5$-$Ca_2Al_2O_5$. Journal of the American Ceramic Society, 85, 1300–1303.

Geller, S., Grant, R.W., and Gonser, U. (1971) Crystal chemistry and magnetic structures of substituted $Ca_2[Fe](Fe)O_5$. Progress in Solid State Chemistry, 5, 1–26.

Hansen, W.C., Brownmiller, L.T., and Bogue, R.H. (1928) Studies on the system calcium oxide-alumina-ferric oxide. Journal of the American Chemical Society, 50, 396–433.

Harchand, U.S., Vishwamitter, B., and Chandra, K. (1984) A study of the iron phase and its hydration behaviour in high alumina cement. Cement and Concrete

Research, 14(1), 19–24.
Kahlenberg, V. and Fischer, R.X. (2000) Crystal growth and cation distribution in doped dicalcium ferrite $Ca_2(Fe_{1-x}Me_x)_2O_5$ (Me = $Al^{3+}$, $Ga^{3+}$). European Journal of Mineralogy, 12, 129–135.
Kahlenberg, V., Fischer, R.X., Weidenthaler, C., and Zeiske, T. (1997). Strukturelle Untersuchungen an $Ca_2Fe_2O_5$ mittels Röntgen- und Neutronenbeugung. European Journal of Mineralogy, 9 Beiheft 2, 147.
Kahlenberg, V., Fischer, R.X., and Shaw, C.S.J. (2000) Rietveld analysis of dicalcium aluminate ($Ca_2Al_2O_5$)—A new high pressure phase with the brownmillerite type structure. American Mineralogist, 85, 1061–1065.
Newkirk, T.F. and Thwaite, J. (1958) Pseudoternary system calcium oxide-monocalcium aluminate ($CaO{\cdot}Al_2O_3$)-dicalcium ferrite ($2CaO{\cdot}Fe_2O_3$). Journal of Research National Bureau of Standards, 61, 233–245.
Rancourt, D.G. and Ping, J.Y. (1991) Voigt-based methods for arbitrary-shape static hyperfine parameter distribution in Mössbauer spectroscopy. Nuclear Instruments and Methods in Physics Research B (NIMB), 58, 85–97.
Rancourt, D.G., McDonald, A.M., Lalonde, A.E., and Ping, J.Y. (1993) Mössbauer absorber thickness for accurate site populations in Fe-bearing minerals. American Mineralogist, 78, 1–7.
Renner, B. and Lehmann, G. (1986) Correlation of angular and bond lengths distortion in $TO_4$ units in crystals. Zeitschrift für Kristallographie, 175, 43–59.
Robinson, K., Gibbs, G.V., and Ribbe, P.H. (1971) Quadratic elongation, a measure of distortion in coordination polyhedra. Science, 172, 567–570.
Rodriguez-Carvajal, J. (2001) Recent developments of the program FULLPROF. Commission on Powder Diffraction (CPD) Newsletter 26, 12–19; http://www.iucr.org/iucr-top/comm/cpd/Newsletters.
Shannon, R.D. and Prewitt, C.T. (1969) Effective ionic radii in oxides and fluorides. Acta Crystallographica, B25, 925–934.
Sheldrick, G.M. (1997a) SHELXS-97. Program for crystal structure refinement. University of Göttingen, Germany.
——— (1997b) SHELXL97. Program for crystal structure refinement. University of Göttingen, Germany.
Smith, D.K. (1962) Crystallographic changes with the substitution of aluminium for iron in dicalcium ferrite. Acta Crystallographica, 15, 1146–1152.
Stoe and Cie (1996) X-SHAPE and X-RED: programs for the optimisation of the crystal shape (w.r.t. the merging R-value) and numerical absorption correction.
Taylor, H.F.W. (1997) Cement chemistry. Thomas Telford, London, 459 p.
Wilson, A.J.C., Ed. (1992) International Tables for Crystallography, vol. C. Mathematical, Physical and Chemical Tables, Kluwer, Dortrecht.
Woermann, E., Eysel, W., and Hahn, T. (1968) Polymorphism and solid solution of the ferrite phase. Proceedings of the 5th International Symposium on the Chemistry of Cement, Part I, 54–60.

MANUSCRIPT RECEIVED MAY 27, 2003
MANUSCRIPT ACCEPTED SEPTEMBER 17, 2003
MANUSCRIPT HANDLED BY SIMONA QUARTIERI